Self-adaptive obstacle crossing of an AntiBot from reconfiguration control and mechanical adaptation

Zhen Song
College of Intelligence Science and Technology, National University of Defense Technology
Changsha 410073, PR China
songzhen15@alumni.nudt.edu.cn

Zirong Luo *
College of Intelligence Science and Technology, National University of Defense Technology
Changsha 410073, PR China
luozirong@nudt.edu.cn

Guowu Wei *
School of Science, Engineering and Environment, University of Salford
Salford M5 4WT, United Kingdom
g.wei@salford.ac.uk

Jianzhong Shang
College of Intelligence Science and Technology, National University of Defense Technology
Changsha 410073, PR China
shangJianzhong@nudt.edu.cn

ABSTRACT

One drawback of wheeled robots is its capability to conquer large obstacles and perform well on complicated terrains, which limits its application in rescue missions. To provide a solution to this issue, an ant-like six-wheeled reconfigurable robot, called AntiBot, is proposed in this paper. The AntiBot has a Sarrus reconfiguration body, a three-rocker-leg passive suspension and mechanical adaptable obstacle-climbing wheeled-legs. In this paper, we demonstrate through simulations and experiments that this robot can

* Corresponding authors

change the position of its centre of mass actively to improve its obstacle crossing capability. The geometric and static stability conditions for obstacle crossing of the robot are derived and formulated, and numerical simulations are conducted to find the feasible region of the robot's configuration in obstacle crossing. In addition, a self-adaptive obstacle crossing algorithm is proposed to improve the robot's obstacle crossing performance. A physical prototype is developed, and based on which a series of experiments are carried out to verify the effectiveness of the proposed self-adaptive obstacle crossing algorithm.

INTRODUCTION

Wheeled mobile robots are the optimal solutions for well-structured environments like roads or flat and regular terrain, which have been widely used in disastrous scenarios with a focus on life detection and rescue [1, 2]. But off-road, their mobility is often limited and highly depends on the type of environments and the size of encountered obstacles [4]. Improving the climbing capability of wheeled rovers requires some special strategies, usually equipping the robot with passive mechanical suspensions, active reconfigurable suspensions or wheel-legged hybrid locomotion units.

Passive suspensions are widely applied in the planetary exploration rovers such as the Spirit and Sojourner [3], the Shrimp [4, 5], the SOLERO [6] and the Jade Rabbit 2 [7]. On the planet's surface characterized by desert, these robots can keep all wheels in contact with the ground through the mechanical adaption provided by passive suspensions, which improves the smoothness of the robot's motion and balances the loads on each wheel. But passive suspensions also increase the size and mass of the robots, making them inconvenient to carry and transport and it is difficult for the robot to climb over vertical obstacles higher than its wheel size.

Robots with active reconfiguration suspensions can actively change their configurations by adjusting the suspension links and joints to improve its motion stability and traction. These robots include the MULE [8], the Crusher [9], the SRR [10, 11], the All-terrain UGV proposed by Zhang et al. [12], and the passive-active hybrid mobile robot presented by Jian et al. [13]. The actively articulated suspension enhances the mobility of the robot but in the meanwhile increases the control complexity and power consumption of the robot, which makes the robot's control system cumbersome.

Wheel-legged hybrid locomotion, commonly attaching wheels to actuated legs like the Octopus [14], the ATHLETE [15, 16], the Hylos [17], and the four-bar wheel-legged rescue robot proposed by Ning et al. [18], is another innovative solution to improve the terrain adaptability and capability of obstacle crossing. Depending on the terrain, these robots can actively regulate their locomotion modes to adjust the position of the centre of mass (COM) and keep all wheels in contact with the ground. But too many joints and wheels that need to be actuated independently makes the control systems complex.

It is obvious that active or hybrid locomotion extends the mobility of a robot but also increases the demands of power and control sources. But in the fields of rescue and planetary exploration, power consumption, complexity and reliability are the predominant criteria used to evaluate the performance of robots [4]. To simplify the control and sensing system, some robots locomote with rotating wheeled-legs. For instance, the Loper [19], the RHex [20], the ASGUARD [21], the FUHAR [22], the TurboQuad [23], the WheeLeR [24], the STEP [25] and the EPI.Q robot [26, 27]. These robots have strong mobility in rugged environments but are constantly subjected to shocks and vibrations because of the rotating legs, which is not conducive to them to carry mission equipment such as cameras.

Combining the virtues of the passive mechanical suspensions, active reconfiguration suspensions and rotating wheeled-leg robots, in this paper we propose an innovative six-wheeled reconfigurable robot called AntiBot, which can realize mechanical self-adaptive obstacle crossing through active reconfiguration control. Compared with the existing robots, there are three superiorities of the AntiBot. First of all, it has a mechanical adaptable three-rocker-leg suspension, which allows the robot to adapt to the undulation of rough terrain passively. Secondly, through reconfiguration and turning the adaptable obstacle-climbing wheeled-legs on both sides, it can cross obstacles higher than the diameter of its wheels adaptively. And the third, the AntiBot can reconfigure itself according to its geometric posture to improve its obstacle crossing capability. This design provides the proposed wheeled robot with powerful climbing capability and a simple control strategy, without any additional terrain sensors. In addition, the mathematical models of the robot's reconfiguration and obstacle crossing are established, and geometric and static stability conditions of the robot's obstacle crossing are derived. An efficient self-adaptive obstacle crossing algorithm is also proposed verified by field experiments.

In this paper, we mainly focus on the modeling of reconfiguration control and obstacle crossing of the AntiBot. In Section 2, we firstly present the design criteria and concept, reconfiguration and mechanical adaption principle of this robot. Then, Section 3 establishes reconfiguration model of this robot, and based on which the kinematic and static analyses of the robot's reconfiguration are conducted. Section 4 presents the geometric and static stability conditions for obstacle crossing of the robot, and simulations are conducted to find the relation between the robot's configuration and obstacle crossing capability. A physical prototype of the robot is developed and an adaptive obstacle crossing algorithm is proposed in Section 5, leading to the obstacle crossing experiments that verifies the effectiveness of the algorithm. Conclusions and future work are addressed in Section 6.

2. MECHANICAL DESIGN OF THE ANTIBOT AND RECONFIGURATION PRINCIPLE

In this section, the design criteria of the AntiBot are firstly proposed, and the detailed mechanical design of the robot is presented.

2.1 Design criteria and concept

The AntiBot is proposed for rescue detection in disastrous fields. It is expected to be a portable robot with light weight, small volume, strong obstacle crossing capability and easy operation. The design criteria are as follows:

1) Light weight. To enable the user to carry the AntiBot with ease, the total weight of the robot is required to be less than 10 kg.
2) Small volume. The AntiBot should be convenient to carry, transport and store. And it can enter the narrow space such as collapsed buildings and earthquake ruins. Hence, the size of the robot is limited within 800 mm × 450 mm × 200 mm.

3) Strong obstacle crossing capability. The AntiBot aims at moving in rugged terrain and climbing over obstacles that is higher than the diameter of its wheels. It should be able to climb over vertical obstacles of about 200 mm height.
4) Easy operation. The AntiBot should be simple to operate. It shall be able to climb over obstacles adaptively without complex operation procedures from the user.

Based on the criteria, and taking the idea of an ant using its two-section body to adjust its posture (Fig. 1(a)), the AntiBot is designed and illustrated in Fig. 1. The robot consists of a reconfigurable two-section body connected by a Sarrus-variant mechanism, two mechanical adaptable obstacle-climbing wheeled-legs and a three-rocker-leg passive suspension (Fig. 1(b)). Through reconfiguration, the robot can be folded up for users to carry on the back (Fig. 1(c)). And by turning the mechanical adaptable obstacle-climbing wheeled-legs, the robot can climb over obstacles higher than the diameter of its wheels (Fig. 1(d)). The operator can send motion commands to the robot and monitor its status information through a handheld ground workstation (Fig. 1(e)).

2.2 Sarrus reconfiguration body

The Sarrus reconfiguration body consists of a front body, a rear body and a Sarrus-variant mechanism (see Fig. 2(a)). The front body is independently driven by two walking wheels, which are propelled by two front DC motors respectively. Two groups of obstacle-climbing wheeled-legs are symmetrically distributed on both sides of the rear body and driven by two rear DC motors separately. The front and rear bodies are connected by a Sarrus-variant mechanism, which provides the relative rotation and foldability between the two bodies. Implemented by the Sarrus-variant mechanism, the robot can realize the reconfiguration of its body.

As shown in Fig. 2, the Sarrus-variant mechanism is a single degree of freedom linkage mechanism, which can convert limited circular motion into linear motion and vice versa [28]. It is constituted of a top plate, a 4-link upper connecting group, a 4-link lower connecting group, a bottom plate, a stepping motor, a connecting shaft, a screw nut and rod. The top plate, the upper and lower connecting groups and the bottom plate are sequentially linked by three sets of parallel revolute joints. The Sarrus-variant mechanism can achieve a linear reciprocating motion with the stepping motor on the top plate driving the bottom plate through the screw rod and nut (see Fig. 2(b) to Fig. 2(d)). Through extension and contraction, the mechanism can change the geometric configuration of the robot (see Fig. 2(e) to Fig. 2(g)). Besides, the top plate of the mechanism also provides a relatively stable installation platform for task equipment such as cameras and life-detectors.

2.3 Mechanical adaptable three-rocker-leg suspension

The robot adopts a three-rocker-leg passive suspension structure, which consists of three parts: the robot’s front body, the left and right mechanical adaptable obstacle-climbing wheeled-legs, as shown in Fig. 3(a). The three-rocker-leg passive suspension provides the robot capability to passively adapt to the fluctuations of the terrain and keep all the six wheels in contact with the ground, which improves the smoothness of the robot’s motion, such as the scenarios shown in Fig. 3(b). Studies on the smoothness of the robot’s motion can refer to another companion robot in Song et al. [29], which has a similar three-rocker-leg passive suspension. This passive suspension structure can effectively reduce the fluctuation of the height of the robot's CoM and slow down the changes of the robot's pitch angle when the robot is crossing obstacles unilaterally.

2.4 Mechanical adaptable obstacle-climbing wheeled-leg

As shown in Fig. 4(a), the obstacle-climbing wheeled-leg contains a parallel-axis gear train driven by a DC motor, a planetary gear train accommodated in the wheeled-leg (planetary gear frame) and two obstacle-crossing wheels fixed on the wheel shafts on both ends of the wheeled-leg.

As shown in Fig. 4(a), the parallel-axis gear train is composed of a motor gear (gear 1 in Fig. 4(b)), a primary gear (dual gear 2 and 2' in Fig. 4(b)) and a secondary gear (gear 3 in Fig. 4(b)). The planetary gear train is constituted of a sun gear (gear 3' in Fig. 4(b)), a planetary frame, four planetary gears (gear 4, 5, 6, 7 in Fig. 4(b)) and a wheel shaft on each side. The secondary gear of the parallel-axis gear train and the sun gear of the planetary gear train rotate synchronously, sharing the same central transmission shaft, to transmit the amplified motor output torque to the wheeled-leg.

When the robot moves on the flat ground, the parallel-axis gear train will be maintained as a fixed-axis gear train. The wheeled-leg will swing with the undulations of the terrain and keep the wheels in contact with the ground to maintain the smoothness of the robot's motion as described in Section 2.3.

When the robot encounters an obstacle, as shown in Fig. 4(c), it takes six steps for it to climb over the obstacle. Step I, firstly, the robot transforms itself into the V-shaped configuration and moves forward until its front walking wheels come into contact with the vertical surface of the obstacle. Step II, the robot keeps moving to increasing the pressure between the front walking wheels and the obstacle's vertical surface. In this case, the friction between the walking wheels and the vertical surface increases gradually and pulls the robot's front body up along the vertical surface. Step III, after the front walking wheels climb onto the upper surface of the obstacle, the robot will continue to move until the front obstacle-crossing wheels contact the vertical surface. Step IV is the most crucial step for the robot to climb over the obstacle, once the obstacle-crossing wheels are blocked by the obstacle, the planetary gear train will be converted into an epicyclic gear train. By setting the transmission ratio i_{73} between the wheel shaft (gear 7 in Fig. 4(b)) and the sun gear (gear 3' in Fig. 4(b)) greater than 1, the amplified motor output torque can drive the wheel-legs to turn around the front obstacle-crossing wheels and prop up the robot's rear body when the front obstacle-crossing wheels are blocked by the obstacle. In the meantime, the front walking wheels keep dragging the robot forward to maintain the obstacle-crossing wheels applying enough pressure to the obstacle's vertical surface. So, the vertical surface can apply sufficient friction to the front obstacle-crossing wheels to prevent them from slipping. Step V, the wheel-legs will flip persistently until the rear obstacle-crossing wheels contact the edge of the obstacle. And Step VI, the robot climbs the obstacle with all the six wheels, leading to the stage that the whole robot comes over the obstacle.

2.5 Comparison with other robots

Take the Antibot into comparison with some typical and novel mobile robots, as shown in Table 1. Some basic features are taken into account to evaluate the robots' obstacle crossing performance [22]. The features include the size, weight, radius and number of wheels, obstacle crossing height and the transformation ratio (the ratio of the maximum obstacle crossing height to the wheels' radius). And the obstacle crossing mechanism and method adopted by the robot are also considered.

It can be seen that the AntiBot has high obstacle crossing height and transformation ratio simultaneously. Compared with the Epi.q-TG which also has rotating wheeled-legs, the AntiBot has higher obstacle crossing height and fewer wheels. And the AntiBot can reconfigure itself autonomously according to its posture to cross obstacles of different heights adaptively, but the Epi.q-TG can't. The STEP can reconfigure its transformable wheels according to the obstacle height, but the trajectory needs to be planned by the operator before. The Quattroped can automatically switch to stair climbing gait or step/bar crossing gait when it confronts the obstacles, but the leg–wheel switching is done manually. The RHyMo can climb obstacle mechanical adaptively, but the novel Rocker-Bogie platform increase the robot's mass and velocity. In comparison, the AntiBot has excellent obstacle crossing performance and can climb obstacles without operators, which has a broad application prospect in disastrous scenarios characterized by uneven terrain and irregularities.

In this section, the design concept of the robot and the mechanical principle of the Sarrus-variant mechanism are illustrated. And the comparison between the AntiBot and some novel mobile robots is taken out. It can be seen that the reconfiguration of the robot mainly depends on the Sarrus-variant mechanism's structural change. To analyze the changes of all wheels' speed and force during the process of the robot's reconfiguration, in the next section, the kinematic and static models of the robot's reconfiguration process are presented. And through numerical simulations, the relationship between the output torque and speed of each motor in the process is obtained to realize the dynamic control of the robot's reconfiguration.

3. MODELING OF RECONFIGURATION CONTROL

The reconfiguration process of the robot is shown in Fig. 5. When the robot is transformed from the flat configuration to the V-shaped configuration, the stepping motor pulls the bottom plate to contract the Sarrus-variant mechanism. At the same time, the output torques of the front motor and the rear motor are opposite, which makes the front walking wheel and the obstacle-crossing wheel move in opposite directions, the wheelbase of the robot is shortened, and the pitch angle of the rear body increases. When the robot transforms itself from the V-shaped configuration to the flat configuration, the Sarrus-variant mechanism is extended, and the wheelbase of the robot is increased.

It can be seen from Fig. 5 that to realize of the robot's reconfiguration, the robot not only needs to control the extension and contraction of the Sarrus-variant mechanism but also needs to control the output of each DC motor. The front and rear motors have to cooperate with the stepping motor in speed and output enough torque to relieve the load on the screw rod so that the stepping motor will not be out of step. Hence, to reveal the relationship between the output torque and speed of each motor, the kinematic and static models are presented in the following sections.

3.1 Kinematic model of reconfiguration

As depicted in Fig. 5, the wheelbase of the robot will be changed when the stepping motor pushes or pulls the Sarrus-variant mechanism to extend or contract. So, the front and rear wheels must also move correspondingly to match the change of the robot's wheelbase. In this section, taking the reconfiguration of the robot on the flat ground as an example, the robot's kinematic model is established to quantitatively describe the changes of the robot's configuration.

Assuming that the robot does not change its motion direction, the robot's reconfiguration is simplified to the motion on a plane for analysis. The main geometrical parameters of the robot are shown in Fig. 6: $O_0\{X_0, Y_0, Z_0\}$ is the fixed coordinate frame, $O_1\{X_1, Y_1, Z_1\}$ is the robot coordinate frame located at the intersection of the centerline of the robot's rear body and the rotation axe of the wheeled-legs on both sides. r is the radii of the front walking wheels and the obstacle-crossing wheels. l_b' is the length of the front and rear body. l_d is the length of the wheelbase. l_e is the length of the wheeled-leg. l_1 is the length of the upper connecting link of the Sarrus-variant mechanism, l_2 is the length of the lower connecting link, and l_3 is the width of the bottom plate of the Sarrus-variant mechanism. δ is the rotation angle of the rear body with respect to the coordinate frame $O_1\{X_1, Y_1, Z_1\}$ in the X_1 - Y_1 plane, which is treated as the variant angle of the robot. δ' is the angle of the upper connecting link relative to the vertical direction.

According to the geometric relationship between the robot and the obstacle, the following formulas can be obtained:

$$\begin{cases} l_d = 2l_b' \cos\delta + l_2 \sin\delta + l_3 \\ l_s = l_2 \cos\delta + l_1 \cos\delta' \end{cases} \tag{1}$$

In Eq. (1), $\sin\delta' = \frac{l_2 \sin\delta}{l_1}$ and $\cos\delta' = \sqrt{1 - \left(\frac{l_2 \sin\delta}{l_1}\right)^2}$. l_s represents the distance between the top and bottom plates of the Sarrus-variant mechanism. The derivative of l_d and l_s with respect to time t can be obtained:

$$\begin{cases} \frac{dl_d}{dt} = -2l_b' \sin\delta \frac{d\delta}{dt} + l_2 \cos\delta \frac{d\delta}{dt} = v_w - v_o \\ \frac{dl_s}{dt} = \left(-l_2 \sin\delta + \frac{(l_2)^2 \sin\delta \cos\delta}{2l_1 \sqrt{(l_1)^2 - (l_2 \sin\delta)^2}}\right) \frac{d\delta}{dt} = v_m \end{cases} \tag{2}$$

where dl_d/dt is the difference (v_w - v_o) between the speed v_w of the robot's front walking wheel and the speed v_o of the obstacle-crossing wheel. dl_s/dt is the feed speed v_m of the screw rod.

Set the rotation speed of the stepping motor to n_m and that of the front walking wheel and the obstacle crossing wheel to n_w and n_o. Then the feed speed of the screw rod is $v_m = pn_m$, where p is the lead of the screw. The speed difference between the front walking wheel and the obstacle crossing wheel is $v_w - v_o = 2\pi r(n_w - n_o)$. The proportional relation k between $n_w - n_o$ and n_m can be obtained as follow

$$k = \frac{n_w - n_o}{n_m} = \frac{p\left(l_2 \cos\delta - 2l_b' \sin\delta\right)}{2\pi r\left(-l_2 \sin\delta + \frac{(l_2)^2 \sin\delta \cos\delta}{2l_1 \sqrt{(l_1)^2 - (l_2 \sin\delta)^2}}\right)} \tag{3}$$

Therefore, as long as the output speed of each motor is set to meet the equation $(n_w - n_o)/n_m = k$, the robot can reconfigure itself during motion and the stepping motor will not be out of step.

3.2 Static model of reconfiguration

In the reconfiguration process, the Sarrus-variant mechanism changes the variant angle δ of the robot by adjusting the length of l_s. Then the front and rear wheels will be pushed or dragged correspondingly to change the robot's wheel base. However, due to the existence of DC motors' holding torques, only relying on the stepping motor in the Sarrus-variant mechanism to push or drag the front and rear wheels is very difficult. Hence, the front and rear DC motors must output appropriate torques simultaneously to reduce the burden of the stepping motor. To reveal the mathematical relationship between the output torques of the stepping motor and DC motors, the static model of the robot's reconfiguration is founded in this section.

Figure 7 shows the static condition of the robot during its transformation from the V-shaped configuration to the flat configuration. Currently, the front motors output anti-clockwise torques to move the front walking wheels forward, the rear motors output clockwise torques to push the obstacle-crossing wheels backward, and the stepping motor pushes the bottom plate vertically downward to extend the Sarrus-variant mechanism.

In Fig. 7, N_1, N_2, N_3 represent the supporting forces of the ground on the robot's front walking wheels, front obstacle-crossing wheels and rear obstacle-crossing wheels respectively. f_1, f_2, f_3 represent the friction forces of the ground against the front walking wheels, the front obstacle-crossing wheels and the rear obstacle-crossing wheels respectively. The output torque of the front motors is T_1 and that of the rear motors is T_2. F_1 is the acting force of the Sarrus-variant mechanism's upper connecting link on the robot's front body, F_{1x} and F_{1y} are the acting forces of the bottom plate on the robot's front body in the horizontal and vertical directions respectively. Because compared with the entire robot, the mass of each part of the Sarrus-mechanism is very small, the upper connecting link on the mechanism can be regarded as a two-force rod by omitting the mass of the Sarrus-variant mechanism. And the direction of the force F_1 is also along the rod. Correspondingly, F_2 is the acting force of the Sarrus-variant mechanism's upper connecting link on the robot's rear body, F_{2x} and F_{2y} are the acting forces of the bottom plate on the robot's rear body in the horizontal and vertical directions respectively. And F_2 also follows the rod direction. m_{fb}, m_{rb}, m_w, m_a represent the mass of the front body, the rear body, the front walking wheel, and that of the wheeled-leg (including the mass of two obstacle-crossing wheels) respectively. m represents the mass of the whole robot and $m = m_{fb} + m_{rb} + 2m_w + 2m_a$. To simplify the analysis, assuming that the robot is reconfiguring in the original position, and then the forces on the robot are balanced in the horizontal direction. And all the wheels are pure rolling, so the wheels are only subject to rolling friction. It can be obtained that

$$f_1 = f_2 + f_3 \tag{4}$$

According to the meshing relationship in Fig. 4(b), the transmission ratio from the sun gear to the obstacle-crossing wheel is i_{37}, the transmission ratio from the motor gear to the sun gear is i_{13}. So, the relationship between the friction torque of the obstacle-crossing wheels and the output torque of the rear motor can be obtained

$$\left(f_2+f_3\right)r=\left(T_2 i_{13}\right)i_{37} \tag{5}$$

Based on the analysis of the static condition of the robot's front body, the following equations can be derived

$$\begin{cases} T_1=f_1 r \\ \left(N_1-2m_w g\right)\left(2l_b'\cos\delta+l_3+l_2\sin\delta\right)+T_1=\left(T_2 i_{13}\right)+m_{fb}g\left(\dfrac{3l_b'\cos\delta}{2}+l_3+l_2\sin\delta\right)+\dfrac{m_{rb}gl_b'\cos\delta}{2} \\ f_1 l_b'\sin\delta+\left(N_1-2m_w g\right)l_b'\cos\delta+T_1=\dfrac{m_{fb}gl_b'\cos\delta}{2}+\dfrac{F_1 l_2\sin\left(\delta+\delta'\right)}{2}+\dfrac{F_{1x}l_2\cos\delta}{2}+\dfrac{F_{1y}l_2\sin\delta}{2} \\ F_{1y}=m_{fb}g+F_1\cos\delta'-\left(N_1-2m_w g\right) \\ F_{1x}=F_1\sin\delta'+f_1 \end{cases} \tag{6}$$

In Eq. (6), the first line represents the torque equilibrium equation of the front walking wheels about point *D*. The second line represents the torque equilibrium equation of the robot about point O_1. The third line represents the torque equilibrium equation of the robot about the connection point (H_1) between the front body and the Sarrus-variant mechanism. The fourth and fifth line represent the static equilibrium equations of the robot's front body in the horizontal and vertical directions, respectively. The following two equations can be derived from Eq. (6).

$$N_1-2m_w g=\frac{\left(T_2 i_{13}\right)-T_1+m_{fb}g\left(\dfrac{3l_b'\cos\delta}{2}+l_3+l_2\sin\delta\right)+\dfrac{m_{rb}gl_b'\cos\delta}{2}}{\left(2l_b'\cos\delta+l_3+l_2\sin\delta\right)} \tag{7}$$

$$\begin{aligned}&\left(N_1-2m_w g\right)\left(l_b'\cos\delta+\frac{l_2\sin\delta}{2}\right)+T_1+f_1\left(l_b'\sin\delta-\frac{l_2\cos\delta}{2}\right)\\&=F_1 l_2\sin\left(\delta+\delta'\right)+\frac{m_{fb}g\left(l_b'\cos\delta+l_2\sin\delta\right)}{2}\end{aligned} \tag{8}$$

In the same way, based on the analysis of the static condition of the robot's rear body, the following equations can be derived

$$\begin{cases} \left(T_2 i_{13}\right) i_{37} = \left(f_2 + f_3\right) r \\ T_2 i_{13} = \left(N_3 - N_2\right) R + \left(f_2 + f_3\right) r \\ \left(N_2 + N_3 - 2m_a g\right)\left(2l_b' \cos\delta + l_3 + l_2 \sin\delta\right) + \left(T_2 i_{13}\right) - T_1 \\ = m_{rb} g \left(\dfrac{3l_b' \cos\delta}{2} + l_3 + l_2 \sin\delta \right) + \dfrac{m_{fb} g l_b' \cos\delta}{2} \\ \left(N_2 + N_3 - 2m_a g\right) l_b' \cos\delta + \left(f_2 + f_3\right) l_b' \sin\delta + \left(T_2 i_{13}\right) \\ = \dfrac{m_{rb} g l_b' \cos\delta}{2} + \dfrac{F_2 l_2 \sin\left(\delta + \delta'\right)}{2} + \dfrac{F_{2y} l_2 \sin\delta}{2} + \dfrac{F_{2x} l_2 \cos\delta}{2} \\ F_{2x} = F_2 \sin\delta' + f_2 + f_3 \\ F_{2y} = m_{rb} g + F_2 \cos\delta' - \left(N_2 + N_3 - 2m_a g\right) \end{cases} \tag{9}$$

In Eq. (9), the first line represents the torque equilibrium equation of the front and rear obstacle crossing wheels about point O_1. The second line represents the torque equilibrium equation of the wheeled-leg about point O_1. The third line represents the torque equilibrium equation of the robot about point D. The fourth line represents the torque equilibrium equation of the robot about the connection point (H_1) between the rear body and the Sarrus-variant mechanism. The fifth and sixth line represent the static equilibrium equations of the robot's rear body in the horizontal and vertical directions, respectively. The following two equations can be derived from Eq. (9).

$$\left(N_2 + N_3 - 2m_a g\right) = \frac{m_{rb} g \left(\dfrac{3l_b' \cos\delta}{2} + l_3 + l_2 \sin\delta \right) + \dfrac{m_{fb} g l_b' \cos\delta}{2} + T_1 - \left(T_2 i_{13}\right)}{\left(2l_b' \cos\delta + l_3 + l_2 \sin\delta\right)} \tag{10}$$

$$\begin{aligned} &\left(N_2 + N_3 - 2m_a g\right)\left(l_b' \cos\delta + \frac{l_2 \sin\delta}{2} \right) + \left(f_2 + f_3\right)\left(l_b' \sin\delta - \frac{l_2 \cos\delta}{2} \right) + \left(T_2 i_{13}\right) \\ &= F_2 l_2 \sin\left(\delta + \delta'\right) + \frac{m_{rb} g \left(l_b' \cos\delta + l_2 \sin\delta\right)}{2} \end{aligned} \tag{11}$$

Equations. (7), (8), (10) and (11) can lead to the following equation

$$\frac{\left(m_{fb}g+m_{rb}g\right)l_b'\cos\delta}{2}+\left(f_1+f_2+f_3\right)\left(l_b'\sin\delta-\frac{l_2\cos\delta}{2}\right)+\left(T_2 i_{13}\right)+T_1=\left(F_1+F_2\right)l_2\sin\left(\delta+\delta'\right) \quad (12)$$

Substituting Eq. (5) and the first line of Eq. (6) into Eq. (12), it can be obtained that

$$\frac{\left(m_{fb}g+m_{rb}g\right)l_b'\cos\delta}{2}+\left(\frac{T_2 i_{13} i_{37}}{r}+\frac{T_1}{r}\right)\left(l_b'\sin\delta-\frac{l_2\cos\delta}{2}\right)+T_2 i_{13}+T_1=\left(F_1+F_2\right)l_2\sin\left(\delta+\delta'\right) \quad (13)$$

Fig. 8 shows the static condition of the Sarrus-variant mechanism, where F_1' is the reaction force of the robot's front body to the upper connecting link, F_{1x}' and F_{1y}' are the horizontal and vertical reaction forces of the front body to the bottom plate respectively. Accordingly, F_2' is the reaction force of the robot's rear body to the upper connecting link, F_{2x}' and F_{2y}' are the horizontal and vertical reaction forces of the rear body to the bottom plate respectively. Similarly, the directions of F_1' and F_2' are also along the upper connecting link. And N_s is the pulling force of the screw to the bottom plate.

According to the static condition of the Sarrus-variant mechanism, there is

$$N_s=\left(F_1'+F_2'\right)\cos\delta' \quad (14)$$

According to Newton's third law, the force and reaction force between the Sarrus-variant mechanism and robot's front and rear bodies are equal in magnitude and opposite in direction, so there is

$$N_s=\left(F_1+F_2\right)\cos\delta' \quad (15)$$

Substitute Eq. (15) into Eq. (13), the pulling force N_{s1} of the screw rod on the top and bottom plates when the robot transforms itself to the flat configuration can be obtained as

$$N_{s1} = \left(F_1 + F_2\right)\cos\delta' = \frac{\left(\frac{\left(m_{fb}g + m_{rb}g\right)l_b'\cos\delta}{2} + \left(\frac{\left(T_2 i_{13}\right)i_{37}}{r} + \frac{T_1}{r}\right)\left(l_b'\sin\delta - \frac{l_2\cos\delta}{2}\right) + \left(T_2 i_{13}\right) + T_1\right)\cos\delta'}{l_2\sin\left(\delta + \delta'\right)} \quad (16)$$

In the light of Eq. (4), Eq. (5) and the first line of Eq. (6), the relationship between the output torque of the front and rear motor can be obtained as

$$T_1 = T_2 i_{13} i_{37} \quad (17)$$

Substitute Eq. (17) into Eq. (16), N_{s1} can be expressed as

$$N_{s1} = \frac{\left(\frac{\left(m_{fb}g + m_{rb}g\right)l_b'\cos\delta}{2} + \frac{2T_1}{r}\left(l_b'\sin\delta - \frac{l_2\cos\delta}{2}\right) + T_1\left(\frac{1}{i_{37}} + 1\right)\right)\cos\delta'}{l_2\sin\left(\delta + \delta'\right)} = \frac{\left(m_{fb}g + m_{rb}g\right)l_b'}{2l_2\left(\tan\delta + \tan\delta'\right)} + T_1\frac{\left(\frac{2\left(l_b'\sin\delta - \frac{l_2\cos\delta}{2}\right)}{r} + \left(\frac{1}{i_{37}} + 1\right)\right)}{l_2\left(\sin\delta + \cos\delta\tan\delta'\right)} \quad (18)$$

Eq. (18) represents the pulling force N_{s1} of the screw rod on the top and bottom plates when the robot transforms itself to the flat configuration. From Eq. (18) we can find that the magnitude of N_{s1} mainly depends on δ and T_1. So, when $T_1 = 0$, it represents the pulling force N_{s0} of the screw rod when the robot is in the natural state. As shown in Fig. 9, at this moment, the front and rear motors will not output torque, and all wheels of the robot will not be subject to friction.

And N_{s0} can be expressed as

$$N_{s0} = \frac{\left(m_{fb}g + m_{rb}g\right)l_b'\cos\delta\cos\delta'}{2l_2\sin\left(\delta + \delta'\right)} = \frac{\left(m_{fb}g + m_{rb}g\right)l_b'}{2l_2\left(\tan\delta + \tan\delta'\right)} \quad (19)$$

Figure 10 shows the static condition of the robot during its transformation to the V-shaped configuration. At this time, the rear motors output anti-clockwise torques to move the obstacle-crossing wheels forward, the front motors output clockwise torques to drag the front walking wheels backward, and the stepping motor pulls up the bottom plate vertically to contract the mechanism.

Compared with the robot's transformation to the flat configuration, the output torques of the front and rear motors are in the opposite directions. Therefore, the front and rear wheels are subject to friction in opposite directions. The pulling force N_{s2} of the screw rod on the top and bottom plates at this time can be obtained as

$$N_{s2} = \frac{\left(\frac{\left(m_{fb} g + m_{rb} g \right) l_b' \cos\delta}{2} - \frac{2T_1}{r}\left(l_b' \sin\delta - \frac{l_2 \cos\delta}{2} \right) - T_1\left(\frac{1}{i_{37}} + 1 \right) \right) \cos\delta'}{l_2 \sin\left(\delta + \delta'\right)} \quad (20)$$

3.3. Reconfiguration simulation

In the previous sections, we have established the mathematical model of the robot's reconfiguration. Reconfiguration of the robot can only be achieved if the output torque and speed of each motor are within the feasible range of its electrical parameters. So, in this section, the numerical simulation is conducted to find the feasible range of the output speed and torque of each motor in the process of reconfiguration.

In this simulation, the geometric and mass parameters of the robot are assigned as: the robot's front body mass m_{fb} = 3.6 kg, rear body mass m_{rb} = 2 kg, front and rear body length l_b' = 220 mm, walking wheel mass m_w = 0.55 kg and radius r = 77.5 mm, mechanical adaptable obstacle-climbing wheeled-leg length l_e = 210 mm and mass m_a =

1.6 kg. The geometrical parameters of the Sarrus-variant mechanism are l_1 = 80 mm, l_2 = 56 mm and l_3 = 51 mm respectively. The transmission ratio between the wheel shaft and the sun gear, denoted as i_{73}, is set to 3.8. The transmission ratio between the motor gear and the secondary gear, denoted as i_{13}, is set to 5.5. The geometric and mass parameters are designed according to the robot's design criteria in Section 2.1.

Firstly, the feasible region of the motors' output speed is analyzed. Substitute the robot's geometric parameters into Eq. (3), the curve of k as a function of δ is illustrated in Fig. 11. It can be seen from the figure that with the increase of the variant angle δ, the proportional coefficient k increases gradually, and the maximum value is about 0.032. In the process of the robot's reconfiguration, if the value of $(n_w - n_o)/n_m$ is less than k, the feed motion of the screw rod will be hindered. However, it is complex to change the output speed of the front and rear motors according to k during the reconfiguration process. So, to simplify the robot's control strategy, if the value of $(n_w - n_o)/n_m$ is set to always greater than 0.032 during the reconfiguration, then the stepping motor can also drive the Sarrus-variant mechanism fluently.

Secondly, the feasible range of the motors' output torque is analyzed. In the process of the robot's reconfiguration, the pulling force N_s of the screw rod determines the output torque of the stepping motor. Set the lead of the screw rod p = 2 mm and the transmission efficiency η = 90%, then the output torque T_m of the stepping motor can be written as

$$T_m = \frac{pN_s}{2\pi\eta} \tag{21}$$

Substitute Eq. (19) into Eq. (21), the holding torque T_{m0} of the stepping motor, when the robot is in its natural state, can be obtained as

$$T_{m0} = \frac{p\left(m_{fb}g + m_{rb}g\right)l_b'}{2l_2\left(\tan\delta + \tan\delta'\right)\left(2\pi\eta\right)} \tag{22}$$

In the same way, when the robot transforms itself into the V-shaped configuration, the output torque T_{m2} of the stepping motor is

$$T_{m2} = \frac{p\left(\frac{\left(m_{fb}g + m_{rb}g\right)l_b'\cos\delta}{2} - \frac{2T_1}{r}\left(l_b'\sin\delta - \frac{l_2\cos\delta}{2}\right) - T_1\left(\frac{1}{i_{37}} + 1\right)\right)\cos\delta'}{2\pi\eta l_2\sin\left(\delta + \delta'\right)} \tag{23}$$

As shown in Fig. 12, take T_1 as 0, 100 mN·m, 300 mN·m, 500 mN·m and 1000 mN·m respectively and draw the curve of T_{m2} as a function of δ. The results show that with the increase of the robot's variant angle δ, the output torque of the stepping motor decreases gradually in the process of the robot transforming itself into the V-shaped configuration. And the larger the torque T_1 output by the front DC motors, the smaller the torque T_{m2} required to be output by the stepping motor. Therefore, in order to lighten the output burden of the screw motor and make the value of T_{m2} less than 0.1 N·m, the value of T_1 should be more than 300 mN·m.

When the robot transforms itself into the flat configuration, the direction of the output torque T_{m1} is the same as that of the output torque T_{m0}. Therefore, as long as $T_{m1} > 0$, the robot can complete the transformation to the flat configuration. We only need to study the magnitude of the pulling force N_{s1} of the screw rod. Take T_1 as 0, 100 mN·m, 300 mN·m, 500 mN·m and 1000 mN·m respectively and make the curve of N_{s1} as a function of δ, as depicted in Fig. 13. As can be seen from the figure, with the decrease of the robot's variant angle δ, the pulling force N_{s1} of the screw rod increases gradually in the process of the robot transforming itself into the flat configuration. And the larger the torque T_1 output by the front DC motors, the larger the value of N_{s1}. Therefore, the output torque of the DC motors should not be too large to prevent the load on the lead screw from exceeding its bearing range.

4. MODELING OF ROBOT SELF-ADAPTIVE OBSTACLE CROSSING

In the previous section, we have established the kinematic and static model of the robot's reconfiguration. Through reconfiguration, the robot improves its capability to climb obstacles. But for obstacle crossing, the robot must satisfy two conditions: the static stability condition and geometric condition. For the static stability, the robot must maintain balance during the whole obstacle-crossing process. For the geometric condition, the robot cannot interfere or collide with obstacles in the process of obstacle crossing. In this section, the static stability and geometric conditions for obstacle crossing are formulated and analyzed to find the relation between the configurations and the obstacle crossing capability of the proposed robot.

4.1 Model of static stability

Referring to Fig. 4(c). III - Fig. 4(c). IV, the robot is most prone to overturn after the front obstacle crossing wheels are blocked by the obstacle, because the pitch angle of the robot is the largest at this time in the whole process. It can be assumed that if the robot can keep balance in this stage, the robot can maintain static stability during the whole process. Therefore, we only need to analyze the static stability of the robot in this obstacle-crossing stage. In this section, the static stability margin (SSM) [30] is used to discuss the static stability of the robot in obstacle-crossing process.

Figure 14 shows the geometry of the robot when its front obstacle crossing wheels are in contact with the obstacle. Compared to the robot's body, the Sarrus-variant mechanism is small in size and has a symmetrical structure. So, it can be assumed that the volume of the mechanism is ignored, and its size is evenly distributed on the front and rear bodies to simplifies the analysis. l_b represents the length of the front and rear body including the Sarrus-variant mechanism's size. d represents the thickness of the robot's body. P_1 represents the centre of mass (CoM) of the robot. C_1 represents the contact point between the front walking wheels and the top surface of the obstacle. C_2 represents the contact point between the front obstacle-crossing wheels and the ground.

The static stability margin (SSM) for a given support polygon is defined as the smallest of the distances from the CoM's projection to the edges of the support polygon, and the static stability condition is SSM > 0 [30]. After the front obstacle crossing wheels are in contact with the obstacle, the stability condition of the robot is secured if the projection of CoM of the robot (P_1) on the X_0-axis, ${}^0x_1$, lies between the contact points C_1 and C_2, that is

$$ {}^0x_{C_2} < {}^0x_1 < {}^0x_{C_1} \tag{24} $$

To solve the inequality, we first find the coordinates of the robot's CoM in the fixed coordinate frame $O_0\{X_0, Y_0, Z_0\}$. For the convenience of analysis, assuming that the

CoM of each part of the robot is at its geometric centre, the expression of the CoM of the robot in the robot coordinate frame $O_1\{X_1, Y_1, Z_1\}$ is

$$ {}^{1}\boldsymbol{P}_1 = \begin{bmatrix} \dfrac{\left(3m_{fb} + m_{rb} + 8m_w\right) l_b \cos\delta}{2m} & \dfrac{\left(m_{fb} + m_{rb}\right) l_b \sin\delta}{2m} & 0 & 1 \end{bmatrix}^T \tag{25} $$

After that, the rotation matrix of the robot coordinate frame $O_1\{X_1, Y_1, Z_1\}$ relative to the fixed coordinate frame $O_0\{X_0, Y_0, Z_0\}$ can be obtained as [31]

$$ \begin{aligned} &\mathbf{R}(\beta,\alpha,\gamma) = Rot(y,\beta)\,Rot(z,\alpha)\,Rot(x,\gamma) \\ &= \begin{bmatrix} \cos\alpha\cos\beta & \sin\beta\sin\gamma - \cos\beta\cos\gamma\sin\alpha & \cos\gamma\sin\beta + \cos\beta\sin\alpha\sin\gamma \\ \sin\alpha & \cos\alpha\cos\gamma & -\cos\alpha\sin\gamma \\ -\cos\alpha\sin\beta & \cos\beta\sin\gamma + \cos\gamma\sin\beta\sin\alpha & \cos\beta\cos\gamma - \sin\beta\sin\alpha\sin\gamma \end{bmatrix} \end{aligned} \tag{26} $$

In Eq. (26), *α*, *β*, *γ* are, respectively, the pitch angle, steer angle and roll angle of the robot. These angles can be detected with the gyroscopic sensors attached to the robot. Let the coordinates of the origin O_1 expressed in the fixed coordinate frame be (*a*, *b*, *c*). The transformation matrix of the robot coordinate frame $O_1\{X_1, Y_1, Z_1\}$ relative to the fixed coordinate frame $O_0\{X_0, Y_0, Z_0\}$ can be obtained in the homogeneous transformation matrix form as

$$ {}^{0}\mathbf{T}_1 = \begin{bmatrix} \cos\alpha\cos\beta & \sin\beta\sin\gamma - \cos\beta\cos\gamma\sin\alpha & \cos\gamma\sin\beta + \cos\beta\sin\alpha\sin\gamma & a \\ \sin\alpha & \cos\alpha\cos\gamma & -\cos\alpha\sin\gamma & b \\ -\cos\alpha\sin\beta & \cos\beta\sin\gamma + \cos\gamma\sin\beta\sin\alpha & \cos\beta\cos\gamma - \sin\beta\sin\alpha\sin\gamma & c \\ 0 & 0 & 0 & 1 \end{bmatrix} \tag{27} $$

In the process of obstacle crossing, the change of the robot's pitch angle *α* is much greater than the roll angle *γ* and the steering angle *β*. By omitting the roll angle *γ* and the steer angle *β*, the robot's centre of mass coordinate expressed in the fixed coordinate frame $O_0\{X_0, Y_0, Z_0\}$ can be obtained as

$$ {}^{0}\boldsymbol{P}_1 = {}^{0}\mathbf{T}_1\,{}^{1}\boldsymbol{P}_1 = \begin{bmatrix} \dfrac{\cos\alpha\left(3m_{fb}+m_{rb}+8m_w\right)l_b\cos\delta}{2m} - \dfrac{\sin\alpha\left(m_{fb}+m_{rb}\right)l_b\sin\delta}{2m} + a \\ \dfrac{\cos\alpha\left(m_{fb}+m_{rb}\right)l_b\sin\delta}{2m} + \dfrac{\sin\alpha\left(3m_{fb}+m_{rb}+8m_w\right)l_b\cos\delta}{2m} + b \\ c \\ 1 \end{bmatrix} = \begin{bmatrix} {}^{0}x_1 \\ {}^{0}y_1 \\ {}^{0}z_1 \\ 1 \end{bmatrix} \quad (28) $$

In the same way, the coordinates of the robot's CoM and the contact points C_1 and C_2 on the X_0 axis of the fixed coordinate frame can be obtained:

$$ {}^{0}x_1 = \frac{\cos\alpha\left(3m_{fb}+m_{rb}+8m_w\right)l_b\cos\delta}{2m} - \frac{\sin\alpha\left(m_{fb}+m_{rb}\right)l_b\sin\delta}{2m} + a \quad (29) $$

$$ {}^{0}x_{C_1} = 2l_b\cos\delta\cos\alpha + a \quad (30) $$

$$ {}^{0}x_{C_2} = \frac{l_e}{2} + a \quad (31) $$

And the relationship between the robot's pitch angle α and obstacle height h can be obtained as

$$ 2l_b\cos\delta\sin\alpha + r = h + r \quad (32) $$

Substitute Eq. (29)-(31) into (24), the static stability condition can be expressed as the following two functions

$$ \begin{aligned} S_1(\alpha) &= {}^{0}x_{C_1} - {}^{0}x_1 \\ &= 2l_b\cos\delta\cos\alpha - \frac{\cos\alpha\left(3m_{fb}+m_{rb}+8m_w\right)l_b\cos\delta}{2m} + \frac{\sin\alpha\left(m_{fb}+m_{rb}\right)l_b\sin\delta}{2m} > 0 \end{aligned} \quad (33) $$

$$ S_2(\alpha) = {}^{0}x_1 - {}^{0}x_{C_2} = \frac{\cos\alpha\left(3m_{fb}+m_{rb}+8m_w\right)l_b\cos\delta}{2m} - \frac{\sin\alpha\left(m_{fb}+m_{rb}\right)l_b\sin\delta}{2m} - \frac{l_e}{2} > 0 \quad (34) $$

Because $\dfrac{\left(\dfrac{3m_{fb}}{4}+\dfrac{m_{rb}}{4}+2m_w\right)}{m}$ is always less than 1 and α is always larger than 0 in this configuration, cos $\alpha > 0$, sin $\alpha > 0$ and $S_1(\alpha) > 0$.

So, the condition of the robot's static stability can be summarized as one function

$$S(\alpha) = {}^0x_1 - {}^0x_{C_2} = \frac{\cos\alpha\left(3m_{fb}+m_{rb}+8m_w\right)l_b\cos\delta}{2m} - \frac{\sin\alpha\left(m_{fb}+m_{rb}\right)l_b\sin\delta}{2m} - \frac{l_e}{2} > 0 \quad (35)$$

where, $\sin\alpha = h/\left(2l_b\cos\delta\right)$ and $\cos\alpha = \sqrt{1-\left(h/\left(2l_b\cos\delta\right)\right)^2}$.

4.2 Model of geometric passing capability

Except the static stability condition, the robot also has to satisfy the geometric condition. When the robot climbs over the obstacle, it should try to avoid the contact between the robot's body and the obstacle before the rear obstacle-crossing wheels touching the obstacle. Even if contact occurs, it should have a mechanism of disengagement, so that the robot has a good geometric passing capability.

According to Fig. 4(c), the robot's body is most prone to touch the edge of the obstacle after the front walking wheels climbing over the obstacle. When the robot's main body collides with the edge of the obstacle, the robot will continue to turn over the wheeled-legs to prop up the rear body because its movement is hindered. When the wheeled-legs are perpendicular to the ground, the CoM of the robot is at the highest position, as shown in Fig. 15.

If the CoM of the robot is higher than the upper surface of the obstacle and within the edge of the obstacle simultaneously at this time, that is, the robot's CoM has climbed over the obstacle, even if the obstacle-crossing wheels cannot touch the edge of the obstacle, the robot can still climb up the obstacle relying on the traction of the front walking wheels. If the robot's CoM is still lower than the height of the obstacle, or outside the edge of the obstacle, the robot cannot move forward anymore. Therefore, in Fig. 15, the geometric condition of robot's obstacle crossing can be expressed as

$$\begin{cases} {}^{0}y_1 > h \\ {}^{0}x_1 > 0 \end{cases} \tag{36}$$

where, (${}^{0}x_1$, ${}^{0}y_1$) represents the coordinates of the robot's CoM in the fixed coordinate frame $O_0\{X_0, Y_0, Z_0\}$ at this time. According to the geometric relationship between the robot and the obstacle, there are

$$\begin{cases} \frac{l_e}{2} + r + 2l_b \cos\delta \sin\alpha = h + r \\ h + \frac{d\cos(\alpha+\delta)}{2} = d_c \sin(\alpha+\delta) + \frac{l_e}{2} + r \\ b = \frac{l_e}{2} + r \\ a = -d_c \cos(\alpha+\delta) - \frac{d\sin(\alpha+\delta)}{2} \end{cases} \tag{37}$$

in which, d_c represents the distance from the contact point between the rear body and the edge of the obstacle to the origin O_1. It can be obtained from Eq. (35) that

$$\begin{cases} d_c = \frac{\left(h + \frac{d\cos(\alpha+\delta)}{2}\right) - \left(\frac{l_e}{2} + r\right)}{\sin(\alpha+\delta)} \\ \sin\alpha = \left(h - \frac{l_e}{2}\right) \Big/ \left(2l_b \cos\delta\right) \\ \cos\alpha = \sqrt{1 - \left(\left(h - \frac{l_e}{2}\right) \Big/ \left(2l_b\cos\delta\right)\right)^2} \end{cases} \tag{38}$$

Substitute Eq. (36) into Eq. (26) and the coordinates of the robot's CoM can be obtained as follow

$$\begin{cases} {}^{0}y_1 = \dfrac{\cos\alpha\left(m_{fb}+m_{rb}\right)l_b\sin\delta}{2m} + \dfrac{\sin\alpha\left(3m_{fb}+m_{rb}+8m_w\right)l_b\cos\delta}{2m} + \dfrac{l_e}{2} + r \\ {}^{0}x_1 = \dfrac{\cos\alpha\left(3m_{fb}+m_{rb}+8m_w\right)l_b\cos\delta}{2m} - \dfrac{\sin\alpha\left(m_{fb}+m_{rb}\right)l_b\sin\delta}{2m} - d_c\cos\left(\alpha+\delta\right) - \dfrac{d\sin\left(\alpha+\delta\right)}{2} \end{cases}$$

(39)

In which, $\alpha+\delta = \arctan\dfrac{\left(\dfrac{l_e}{2}+r\right)-\left(h+\dfrac{d}{2}\cos\left(\alpha+\delta\right)\right)}{\left(a+\dfrac{d}{2}\sin\left(\alpha+\delta\right)\right)}$.

Only when the robot's CoM is higher than the upper surface of the obstacle and within the edge of the obstacle simultaneously, the robot satisfies the geometric condition of obstacle crossing. Substitute Eq. (39) into Eq. (36), the geometric condition of the robot's obstacle crossing can be expressed as two functions about *α*:

$$G_1\left(\alpha\right) = \frac{\cos\alpha\left(m_{fb}+m_{rb}\right)l_b\sin\delta}{2m} + \frac{\sin\alpha\left(3m_{fb}+m_{rb}+8m_w\right)l_b\cos\delta}{2m} + r - 2l_b\cos\delta\sin\alpha > 0 \quad (40)$$

$$G_2\left(\alpha\right) = \frac{\cos\alpha\left(3m_{fb}+m_{rb}+8m_w\right)l_b\cos\delta}{2m} - \frac{\sin\alpha\left(m_{fb}+m_{rb}\right)l_b\sin\delta}{2m} - d_c\cos\left(\alpha+\delta\right) - \frac{d\sin\left(\alpha+\delta\right)}{2} > 0$$

(41)

where, $\sin\alpha = \left(h-\dfrac{l_e}{2}\right)\Big/\left(2l_b\cos\delta\right)$, $\cos\alpha = \sqrt{1-\left(\left(h-\dfrac{l_e}{2}\right)\Big/\left(2l_b\cos\delta\right)\right)^2}$.

4.3. Obstacle crossing numerical simulation

In the previous sections, with respect to the pitch angle α, the geometric and static stability condition for obstacle crossing of the proposed mobile robot are derived and formulated in functions as $S(\alpha) > 0$, $G_1(\alpha) > 0$, and $G_2(\alpha) > 0$. As long as these inequalities are satisfied simultaneously, the robot's obstacle crossing capability can be secured. In this section, set the robot's geometric and mass parameters are the same as that mentioned in Section 3.3, and simulation is conducted to find the feasible region of δ where the robot can cross the obstacle.

According to Eq. (35), when $S(\alpha) = 0$, δ is the maximum variant angle δ_{max0} of the robot satisfying the static stability condition at the current pitch angle α. Solving the implicit function of equation $S(\alpha) = 0$ by using MATLAB®, the curve of δ_{max0} as a function of α can be obtained and illustrated in Fig. 16. The shadowed part in the figure is the feasible region of δ where the robot can satisfy the static stability condition.

According to Eq. (40) and Eq. (41), when $G_1(\alpha) = 0$ and $G_2(\alpha) = 0$, δ is the minimum variant angle δ_{min0} of the robot satisfying the geometric condition at the current pitch angle α. Solving the implicit function of equation $G_1(\alpha) = 0$ and $G_2(\alpha) = 0$ by using MATLAB®, the curves of δ_{min0} as a function of α is obtained and shown in Fig. 17. The shadowed part in the figure is the feasible region of δ where the robot can satisfy the geometric condition.

From Fig. 16 and Fig. 17, it can be found that in the process of obstacle crossing, the feasible range of the robot's variant angle δ changes with the variation of the robot's pitch angle α. If the robot can dynamically adjust the variant angle δ according to the value of α, it's obstacle crossing capability will be guaranteed. Hence, a self-adaptive obstacle crossing algorithm is proposed in the next section, which enables the robot to dynamically control its geometric posture and keep itself satisfying the obstacle crossing conditions.

5. PHYSICAL PROTOTYPE, CONTROL ALGORITHM AND OBSTACLE-CROSSING EXPERIMENTS

Based on the mechanical design, analysis and numerical simulation of the proposed robot's reconfiguration and obstacle crossing are presented in the previous sections. In this section, a physical prototype of the proposed robot is developed. A self-adaptive obstacle crossing algorithm is proposed, and experiments are conducted to verify the effectiveness of the control algorithm.

5.1. Prototype development

Based on the mechanical structure presented above, adopting the structure parameters in Table 2, with some essential adjustments required from mechanical component design, a physical prototype of the proposed robot was developed as shown in Fig. 18. The robot's overall dimensions are 780 mm (length) × 454 mm (width) × 190 mm (height) and overall mass is 9.9 kg, including a 24 V lithium battery to power the whole robot.

The robot's control strategy is shown in Fig. 19. The operator firstly sends motion commands to the robot, which are decoded by the signal receiver and then transmitted to the robot's posture control centre. Then the control centre sends the PWM signals to the robot's motors through the driving components. In the meantime, each DC motor feeds back its actual speed to the control center to realize the PID closed-loop control of the robot's motion.

The robot's maximum speed can reach 0.5m/s, when it moves on the flat ground. When the robot moves on the uneven ground such as sand (Fig. 20(a)) and grass (Fig. 20(b)), it usually increases its variant angle to raise its center of gravity. And its unique three-rocker-leg passive suspension also enables the robot to keep six wheels in contact with the ground, which maintains the smoothness of the robot's movement. The robot turns through the differential speed movement of the wheels on both sides. The robot usually shortens its wheelbase by raising the posture to facilitate better steering (Fig. 20(c)).

5.2. Reconfiguration capability verification

In Section 3.3, through the numerical simulation we have got the maximum value of the proportional coefficient k. According to the simulation results in Fig. 11, if the speeds of front and rear wheels satisfy $(n_w – n_o)/n_m > 0.032$, the screw motor will not be out of step and the Sarrus-variant mechanism can stretch and contract smoothly. To simplify the control algorithm, the front walking wheels and the obstacle crossing wheels are set to move in the opposite direction at the same speed, i.e., $n_w = – n_o$. And keep $(n_w – n_o)/n_m > 0.032$, the reconfiguration experiment is carried out as shown in Fig. 21. The robot can switch its geometric posture between the flat configuration and the V-shape configuration, and the stepping motor does not lose step.

5.3. Self-adaptive obstacle crossing algorithm and experiments

As mentioned at the end of Section 4.3, to make the robot's configuration satisfy both the geometric and stability conditions in the process of obstacle crossing, we have developed a self-adaptive obstacle crossing algorithm. The algorithm enables the robot to detect its own posture during the movement and make adjustments in time to ensure its obstacle crossing capability.

As shown in Fig. 22, the robot mainly carries out real-time detection on its front body pitch angle δ_f and rear body pitch angle δ_r to judge its own geometric posture, which are measured by two nine-axis sensors JY901 (WitMotion®, China). According to the geometric relationship between the robot and obstacle, it can be obtained that

$$\begin{cases} \delta_f = \delta - \alpha \\ \delta_r = \delta + \alpha \end{cases} \tag{42}$$

According to Fig. 16 and Fig. 17, the robot must satisfy the following inequation for obstacle crossing:

$$\delta_{\min 0} < \delta < \delta_{\max 0} \tag{43}$$

Substitute Eq. (42) into Eq. (43), the obstacle crossing conditions can be summarized as the following inequations:

$$\begin{cases} \delta_f > \delta_{\min 0} - \alpha \\ \delta_r < \delta_{\min 0} + \alpha \end{cases} \tag{44}$$

From Fig. 16 and Fig. 17, it can be obtained that the maximum value of $\{\delta_{\min0} - \alpha\}$ is about 8° and that of $\{\delta_{\max0} + \alpha\}$ is about 60°. If the robot can always keep δ_f > 8° and δ_r < 60°, the robot can satisfy the stability and geometric conditions simultaneously. The algorithm is set up as: the two nine-axis sensors detect the values of δ_f and δ_r in real time, and the robot makes timely adjustments to the variant angle δ, according to its geometric posture. Considering the measurement error of the sensor, we set $\delta_{f\min}$ = 10° as the safety threshold for the robot to satisfy the geometric condition and $\delta_{r\max}$ = 70° as the safety threshold for the robot to satisfy the stability condition. Consequently, once δ_f is less than 10°, the robot will increase the variant angle δ. And once δ_r is more than 70°, the robot will decrease the variant angle δ. The flow of robot's self-adaptive obstacle crossing algorithm is indicated in the diagram in Fig. 23 and is implanted in the proposed physical prototype.

Based on the prototype, a series of field tests were carried out to check and verify the performance of the robot's self-adaptive obstacle crossing algorithm. The experiments on the robot crossing 200 mm high vertical obstacles were carried out. Firstly, the robot climbed over the obstacle without enabling the self-adaptive obstacle crossing algorithm. As show in Fig. 24, when the robot was climbing the obstacle in the flat configuration, i.e., δ_f = 0, its body's chassis would contact the edge of the obstacle and prevent it from crossing the obstacle. The obstacle-climbing wheeled-legs keep flipping, but could not make the obstacle-crossing wheels touch the top surface of the obstacle and pull the robot. So, when the robot does not satisfy the geometric condition, the robot cannot climb over the obstacle.

As shown in Fig. 25, when the pitch angle δ_r of the robot's rear body exceeded the safety threshold, the robot would lose stability and turnover during the process of obstacle crossing without enabling the self-adaptive obstacle crossing algorithm. So, when the robot does not satisfy the static stability condition, the robot cannot climb over the obstacle.

Then the self-adaptive obstacle crossing algorithm of the robot was enabled. To verify that the algorithm can keep the robot satisfying the geometric condition, the variant angle δ was set at about 20° before obstacle crossing, and then the robot's self-adaptive obstacle crossing algorithm was enabled. As shown in Fig. 26(a), the robot would continuously increase its variant angle δ during the obstacle crossing process to prevent the chassis of the car body from contacting the edge of the obstacle. Fig. 26(b) shows the curves of δ_f and δ_r as functions of time. It can be seen that during the obstacle crossing process, once the front body's pitch angle δ_f was less than 10°, the robot would increase the variant angle until δ_f was within the safety threshold.

Similarly, to verify that the algorithm can keep the robot satisfying the stability condition, the variant angle δ was set about 45° before obstacle crossing, and then the robot's self-adaptive obstacle crossing algorithm was started. As shown in Fig. 27(a), in the process of obstacle crossing, when the pitch angle δ_r of the rear body exceeded the safety threshold, the robot would actively decrease its variant angle δ to avoid overturning. Fig. 27(b) shows the curves of δ_f and δ_r as functions of time. It can be found that once the rear body's pitch angle δ_r was more than 70° the robot would decrease the variant angle until δ_r was within the safety threshold, which proved that the self-adaptive obstacle crossing algorithm can make the robot maintain the stability.

Besides, the experiments of climbing stairs (Fig. 28) and crossing side obstacles (Fig. 29) were carried out. During climbing stairs, the robot continuously rotated the wheel-legs to support itself and the front walking wheels always kept contact with the stair surface to pull the robot forward. During crossing the side obstacle, it can be seen that, relying on its three-rocker-leg passive suspension, when one side of the robot passes over obstacles, the wheels on the other side can also maintain contact with the ground, ensuring the stability of the robot.

The experiments accomplished here not only verify the obstacle crossing performance of the proposed robot but also show the fact that the self-adaptive obstacle crossing algorithm improve the robot's obstacle crossing capability. Through detecting and adjusting its own posture, the robot can maintain the geometric passing capability and static stability during the obstacle crossing process.

6. CONCLUSIONS

This paper proposed and discussed a novel six-wheeled robot, i.e., AntiBot, with a reconfigurable body and self-adaptive obstacle-crossing mechanisms. By turning the adaptive obstacle-climbing wheeled-legs, the robot can climb over obstacles of different heights. Through stretching or contracting the Sarrus-variant mechanism, the robot can transform itself to different configurations to improve its obstacle crossing capability.

The mechanical design of the proposed robot was presented. Based on the mechanical design, the mathematical models of the robot's reconfiguration and obstacle crossing were established. Numerical simulations were conducted to find the feasible ranges of each motor's output torque and speed. Subsequently, geometric and static stability conditions of the robot's obstacle crossing were derived, and simulations were carried out to characterize the feasible region of the robot's variant angle for obstacle crossing.

Further, a physical prototype of the proposed mobile robot was developed, and based on the previous simulations, a self-adaptive obstacle crossing algorithm was proposed, which makes the robot being able to maintain the geometric passing capability and motion stability during the obstacle crossing process, through detecting and adjusting its geometric posture. Experiments were subsequently carried out to prove the obstacle crossing performance of the robot and the effectiveness of the self-adaptive obstacle crossing algorithm.

Further research will be focused on the development of an automatic navigation system and a robust mechanical structure to improve the reliability of the robot in rugged environments.

NOMENCLATURE

I	all variables should appear in italics
tl	two-letter abbreviations should appear in italics
tla	three-letter abbreviations should not appear in italics
Re	Reynolds number and similar abbreviations do not use italics
T	use the “Tab” key to add more rows to this table
$O_0\{X_0, Y_0, Z_0\}$	fixed coordinate frame
$O_1\{X_1, Y_1, Z_1\}$	robot coordinate frame located at the intersection of the centerline of the robot’s rear body and the rotation axe of the wheeled-legs on both sides
r	radii of the front walking wheels and the obstacle-crossing wheels
l_b'	length of the front and rear body
l_d	length of the wheelbase
l_e	length of the wheeled-leg
l_1	length of the upper connecting link of the Sarrus-variant mechanism
l_2	length of the lower connecting link of the Sarrus-variant mechanism
l_3	width of the bottom plate of the Sarrus-variant mechanism
δ	rotation angle of the rear body with respect to the coordinate frame $O_1\{X_1, Y_1, Z_1\}$ in the X_1 - Y_1 plane (variant angle of the robot)
δ'	angle of the upper connecting link relative to the vertical direction

l_s	distance between the top and bottom plates of the Sarrus-variant mechanism
dl_d/dt	difference (v_w - v_o) between the speed v_w of the robot's front walking wheel and the speed v_o of the obstacle-crossing wheel
dl_s/dt	feed speed v_m of the screw rod
n_m	rotation speed of the stepping motor
n_w	rotation speed of the front walking wheel
n_o	rotation speed of the obstacle crossing wheel
p	lead of the stepping motor screw
k	proportional relation between n_w - n_o and n_m
N_1	supporting forces of the ground on the robot's front walking wheels
N_2	supporting forces of the ground on the robot's front obstacle-crossing wheels
N_3	supporting forces of the ground on the robot's rear obstacle-crossing wheels
f_1	friction forces of the ground against the front walking wheels
f_2	friction forces of the ground against the front obstacle-crossing wheels
f_3	friction forces of the ground against the rear obstacle-crossing wheels
T_1	output torque of the front motors
T_2	output torque of the rear motors

F_1	acting force of the Sarrus-variant mechanism's upper connecting link on the robot's front body
F_{1x}	acting forces of the bottom plate on the robot's front body in the horizontal direction
F_{1y}	acting forces of the bottom plate on the robot's front body in the vertical direction
F_2	acting force of the Sarrus-variant mechanism's upper connecting link on the robot's rear body
F_{2x}	acting forces of the bottom plate on the robot's rear body in the horizontal direction
F_{2y}	acting forces of the bottom plate on the robot's rear body in the vertical directions
m_{fb}	mass of the front body
m_{rb}	mass of the rear body
m_w	mass of the front walking wheel
m_a	mass of the wheeled-leg (including the mass of two obstacle-crossing wheels)
m	mass of the whole robot and $m = m_{fb} + m_{rb} + 2m_w + 2m_a$
i_{37}	transmission ratio from the sun gear to the obstacle-crossing wheel
i_{13}	transmission ratio from the motor gear to the sun gear

T_1	output torque of the front motors
T_2	output torque of the rear motors
F_1'	reaction force of the robot's front body to the upper connecting link
F_{1x}'	horizontal reaction force of the front body to the bottom plate
F_{1y}'	vertical reaction force of the front body to the bottom plate
F_2'	reaction force of the robot's rear body to the upper connecting link
F_{2x}'	horizontal reaction force of the rear body to the bottom plate
F_{2y}'	vertical reaction force of the rear body to the bottom plate
N_s	pulling force of the screw to the bottom plate
N_{s1}	pulling force of the screw rod on the top and bottom plates when the robot transforms itself to the flat configuration
N_{s0}	pulling force of the screw rod when the robot is in the natural state
N_{s2}	pulling force N_{s2} of the screw rod on the top and bottom plates when the robot transforms itself to the V-shaped configuration
η	the transmission efficiency of the screw rod
T_{m0}	holding torque of the stepping motor, when the robot is in its natural state
T_{m1}	output torque of the stepping motor, when the robot transforms itself into the flat configuration
T_{m2}	the output torque T_{m2} of the stepping motor, when the robot transforms itself into the V-shaped configuration

l_b	length of the front and rear body including the Sarrus-variant mechanism's size
d	thickness of the robot's body
P_1	centre of mass (CoM) of the robot
C_1	contact point between the front walking wheels and the top surface of the obstacle
C_2	contact point between the front obstacle-crossing wheels and the ground
α	pitch angle of the robot
β	steer angle of the robot
γ	roll angle of the robot
(a, b, c)	coordinates of the origin O_1 expressed in the fixed coordinate frame
h	obstacle height
$S(\alpha)$	static stability condition of the robot's obstacle crossing
d_c	distance from the contact point between the rear body and the edge of the obstacle to the origin O_1
$G_1(\alpha)$, $G_2(\alpha)$	the geometric condition of the robot's obstacle crossing
$\delta_{\max 0}$	maximum variant angle of the robot satisfying the static stability condition at the current pitch angle α
$\delta_{\min 0}$	minimum variant angle of the robot satisfying the geometric condition at the current pitch angle α

δ_f	robot's front body pitch angle
δ_r	robot's rear body pitch angle

REFERENCES

[1] Tadokoro, S., Takamori, T., Tsurutani, S. and Osuka, K., 1997, "*On Robotic Rescue Facilities for Disastrous Earthquakes -From the Great Hanshin-Awaji (Kobe) Earthquake*," Journal of Robotics Mechatronics, **9**(1), pp. 46-56. DOI: 10.20965/jrm.1997.p0046

[2] Casper, J. and Murphy, R.R., 2003, "*Human-robot interactions during the robot-assisted urban search and rescue response at the World Trade Center*," IEEE Transactions on Systems Man Cybernetics Part B Cybernetics A Publication of the IEEE Systems Man Cybernetics Society, **33**(3), pp. 367. DOI: 10.1109/TSMCB.2003.811794

[3] Lindemann, R.A. and Voorhees, C.J., 2005, "*Mars Exploration Rover mobility assembly design, test and performance*," IEEE International Conference on Systems, Man and Cybernetics, **1**(1), pp. 450-455. DOI: 10.1109/ICSMC.2005.1571187

[4] Siegwart, R., Lamon, P., Estier, T., Lauria, M. and Piguet, R., 2000, "*Innovative design for wheeled locomotion in rough terrain*," Robotics Autonomous Systems, **40**(2-3), pp. 151-162. DOI: 10.1016/S0921-8890(02)00240-3

[5] Estier, T., Crausaz, Y., Merminod, B., Lauria, M., Piguet, R. and Siegwart, R., 2000, "*An Innovative Space Rover with Extended Climbing Abilities*," Robotics, **2000**(1), pp. 333-339. DOI: 10.1016/S0921-8890(02)00240-3

[6] Michaud, S., Schneider, A., Bertrand, R., Lamon, P., Siegwart, R., Van Winnendael, M. and Schiele, A., 2002, "*SOLERO : Solar Powered Exploration Rover*," Symposium on Advanced Space Technologies for Robotics and Automation (ASTRA), Noordwijk, NL, **7**. DOI: 10.3929/ethz-a-010090926

[7] Zhang, Y., Xiao, J., Zhang, X., Liu, D. and Zou, H., 2014, "*Design and implementation of Chang'E-3 rover location system*," Scientia Sinica Technologica, **44**(5), pp. 483. DOI: 10.1360/092014-50

[8] Heimfarth, T., Araujo, J.P.D., and Giacomin, J.C., 2014, "*Unmanned Aerial Vehicle as Data Mule for Connecting Disjoint Segments of Wireless Sensor Network with Unbalanced Traffic*," 2014 IEEE 17th International Symposium on Object/Component/Service-Oriented Real-Time Distributed Computing, Reno, NV, pp. 246-252. DOI: 10.1109/ISORC.2014.51

[9] Fish, S. and Sitzman, A., 2009, "*Unmanned Vehicles for Mobile Electromagnetic Launch Platforms*," IEEE Transactions on Magnetics, **45**(1), pp. 639-640. DOI: 10.1109/TMAG.2008.2008869

[10] Iagnemma, K., Rzepniewski, A., Dubowsky, S., Pirjanian, P., Huntsberger, T. and Schenker, P. 2000, "*Mobile robot kinematic reconfigurability for rough terrain*," Sensor

Fusion and Decentralized Control in Robotic Systems III, Boston, MA, **4196**, . DOI: 10.1117/12.403739

[11] Kozma, R., Huntsberger, T., Aghazarian, H. and Freeman, W. J., 2007, "*Implementing intentional robotics principles using SSR2K platform*," 2007 IEEE/RSJ International Conference on Intelligent Robots and Systems, San Diego, CA, pp. 2262-2267. DOI: 10.1109/IROS.2007.4399490

[12] Zhang, T., Wang, T., Wu, Y. and Zhao, Q., 2013, "*Design and Realization of an All-terrain Unmanned Ground Vehicle*," ROBOT, **35**(6), pp. 657-664. DOI: 10.3724/SP.J.1218.2013.00657

[13] Jiang, H., Xu, G., Zeng, W. and Gao, F., 2019, "*Design and kinematic modeling of a passively-actively transformable mobile robot*," Mechanism Machine Theory, **142**(2), pp. 103591. DOI: 10.1016/j.mechmachtheory.2019.103591

[14] Lauria, M., Piguet, Y., and Siegwart, R., 2002, "*Octopus - An Autonomous Wheeled Climbing Robot*," The Fifth International Conference on Climbing and Walking Robots (CLAWAR). DOI: 10.3929/ethz-a-010098355

[15] Wilcox, B.H., 2011, "*ATHLETE: A cargo-handling vehicle for solar system exploration*," 2011 Aerospace Conference, Big Sky, MT, pp. 1-8. DOI: 10.1109/AERO.2011.5747494

[16] Sunspiral, V., Wheeler, D.W., Chavez-Clemente, D. and Mittman, D., 2012, "*Development and field testing of the FootFall planning system for the ATHLETE robots*," Journal of Field Robotics, 2**9**(3), pp. 483-505. DOI: 10.1002/rob.20410

[17] Grand, C., Benamar, F., and Plumet, F., 2010, "*Motion kinematics analysis of wheeled-legged rover over 3D surface with posture adaptation*," Mechanism Machine Theory, **45**(3), pp. 477-495. DOI: 10.1016/j.mechmachtheory.2009.10.007

[18] Ning, M., Xue, B., Ma, Z., Zhu, C., Liu, Z., Zhang, C., Wang, Y. and Zhang, Q., 2018, " *Design and analysis for a multifunctional rescue robot with four-bar wheel-legged structure*," Advances in Mechanical Engineering, **10**(2), pp. 1-14. DOI: 10.1177/1687814017747399

[19] Herbert, S.D., Drenner, A., and Papanikolopoulos, N., 2008, "*Loper: A quadruped-hybrid stair climbing robot*," 2008 IEEE International Conference on Robotics and Automation, pp. 799-804. DOI: 10.1109/ROBOT.2008.4543303

[20] Altendorfer, R., Moore, N., Komsuoglu, H., Buehler, M., Brown, H.B., Jr., McMordie, D., Saranli, U., Full, R. and Koditschek, D.E., 2001, "*RHex: A Biologically Inspired Hexapod Runner*," Autonomous Robots, **11**(3), pp. 207-213. DOI: 10.1023/A:1012426720699

[21] Eich, M., Grimminger, F. and Kirchner, F., 2009, "*Adaptive compliance control of a multi-legged stair-climbing robot based on proprioceptive data*," Industrial Robot, **36**(4), pp. 331-339. DOI: 10.1108/01439910910957084

[22] Mertyüz, R., Tanyldz, A. K., Taar, B., Tatar, A. B. and Yakut, O., 2020, "*FUHAR: A transformable wheel-legged hybrid mobile robot*," Robotics Autonomous Systems, **133**, 103627. DOI: 10.1016/j.robot.2020.103627

[23] Chen, W.H., Lin, H.S., Lin, Y.M. and Lin, P.C., 2017, " *TurboQuad: A Novel Leg–Wheel Transformable Robot With Smooth and Fast Behavioral Transitions*," IEEE Transactions on Robotics, **33**(5), pp. 1025-1040. DOI: 10.1109/TRO.2017.2696022

[24] Zheng, C. and Lee, K., 2019, "*WheeLeR: Wheel-Leg Reconfigurable Mechanism with Passive Gears for Mobile Robot Applications*," 2019 International Conference on Robotics and Automation (ICRA), Montreal, QC, pp. 9292-9298. DOI: 10.1109/ICRA.2019.8793686

[25] Kim, Y., Lee, Y. and Lee, S., 2020, "*STEP: A New Mobile Platform With 2-DOF Transformable Wheels for Service Robots*," IEEE/ASME Transactions on Mechatronics, **25**(4), pp. 1859-1868. DOI: 10.1109/TMECH.2020.2992280

[26] Quaglia, G. and Nisi, M., 2015, "*Design and Construction of a New Version of the Epi.q UGV for Monitoring and Surveillance Tasks*," ASME 2015 International Mechanical Engineering Congress and Exposition, Houston, Texas, **50163**. DOI: 10.1115/IMECE2015-50163

[27] Quaglia, G., Oderio, R., Bruzzone, L. and Razzoli, R. P., 2011, "*Epi.q Mobile Robots Family*," Asme International Mechanical Engineering Congress & Exposition, pp. 1165-1172. DOI: 10.1115/IMECE2011-62674

[28] Chen, G., Zhang, S. and Li, G., 2013, "*Multistable Behaviors of Compliant Sarrus Mechanisms*," Journal of Mechanisms Robotics, **5**(2), pp. 021005-1-021005-10. DOI: 10.1115/1.4023557

[29] Song, Z., Luo, Z., Wei, G. and Shang, J., 2021, "*Design and analysis of a six-wheeled companion robot with mechanical obstacle-overcoming adaptivity*," Mechanical Sciences, **12**(2), pp. 1115-1136. DOI: 10.5194/ms-12-1115-2021

[30] Garcia, E., Estremera, J. and Santos, P., 2002, "*A comparative study of stability margins for walking machines*," Robotica, **20**(6), pp. 595-606. DOI: 10.1017/S0263574702004502

[32] Liu, C., 2018, "*Research on obstacle-performance of articulated-track inspection robot under complex environment*," Master of Engineering, University of South China, Hengyang, P.R.China.

[33] Quaglia, G., Bruzzone, L., Bozzini, G., Oderio, R. and Razzoli, R.P., 2011, "*Epi.q-TG: mobile robot for surveillance*," Industrial Robot, **38**(3), pp. 282-291. DOI: 10.1108/01439911111122789

[34] Kim, K., Kim, Y., Kim, J., Kim, H. and Seo, T., 2020, "*Optimal Trajectory Planning for 2-DOF Adaptive Transformable Wheel*," IEEE Access, **8**, pp. 14452-14459. DOI: 10.1109/ACCESS.2020.2966767

[35] Chen, S.C., Huang, K.J., Chen, W.H., Shen, S.Y., Li, C.H. and Lin, P.C., 2014, "*Quattroped: A leg-wheel transformable robot*," IEEE/ASME Transactions on Mechatronics, **19**(2), pp. 730-742. DOI: 10.1109/TMECH.2013.2253615

[36] Chen, S.C., Huang, K.J., Li, C.H. and Lin, P.C., 2011, "*Trajectory planning for stair climbing in the leg-wheel hybrid mobile robot quattroped*," 2011 IEEE International Conference on Robotics and Automation, Shanghai, China, pp. 1229-1234. DOI: 10.1109/ICRA.2011.5980091

[37] Choi, D., Kim, Y., Jung, S., Kim, J. and Kim, H., 2016, " *A new mobile platform (RHyMo) for smooth movement on rugged terrain*," IEEE/ASME Transactions on Mechatronics, **21**(3), pp. 1303-1314. DOI: 10.1109/TMECH.2016.2520085

[38] Choi, D., Kim, Y., Jung, S., Kim, H. and Kim, J., 2016, "*Improvement of step-climbing capability of a new mobile robot RHyMo via kineto-static analysis*," Mechanism & Machine Theory, **114**, pp. 20-37. DOI: 10.1016/j.mechmachtheory.2017.03.018

[39] Jung, S., Choi, D., Kim, H. and Kim, J., 2016, "*Trajectory generation algorithm for smooth movement of a hybrid-type robot Rocker-Pillar(Article)*," Journal of Mechanical Science and Technology, **30**(11), pp. 5217-5224. DOI: 10.1108/01439911111122789

Figure Captions List

Fig. 1	The design, configurations and control of the AntiBot. a) The two-section body of the ant; b) the appearance of the robot; c) the robot is carried by the user on the back; d) the robot climbs obstacles higher than itself; e) the handheld ground workstation
Fig. 2	Mechanical structure of the Sarrus reconfiguration body. a) The composition of the Sarrus reconfiguration body; b) The Sarrus-variant mechanism is in the extended state; c) the structure of the Sarrus-variant mechanism; d) the Sarrus-variant mechanism is in the contraction state; e) the flat configuration; f) the V-shaped configuration; g) the folded configuration
Fig. 3	The mechanical adaptable three-rocker-leg suspension. (a) The composition of the three-rocker-leg suspension; (b) terrain adaptability of the robot.
Fig. 4	The structure and transmission of the wheeled-leg and the obstacle-crossing process of the robot. a) The mechanical structure of the wheeled-leg; b) the gear transmission diagram in the wheeled-leg; c) the obstacle crossing process of the robot
Fig. 5	The reconfiguration process of the robot
Fig. 6	Main geometrical parameters of the robot

Table Caption List

Information Regarding Figures and Tables

Fig. 1

Fig .2

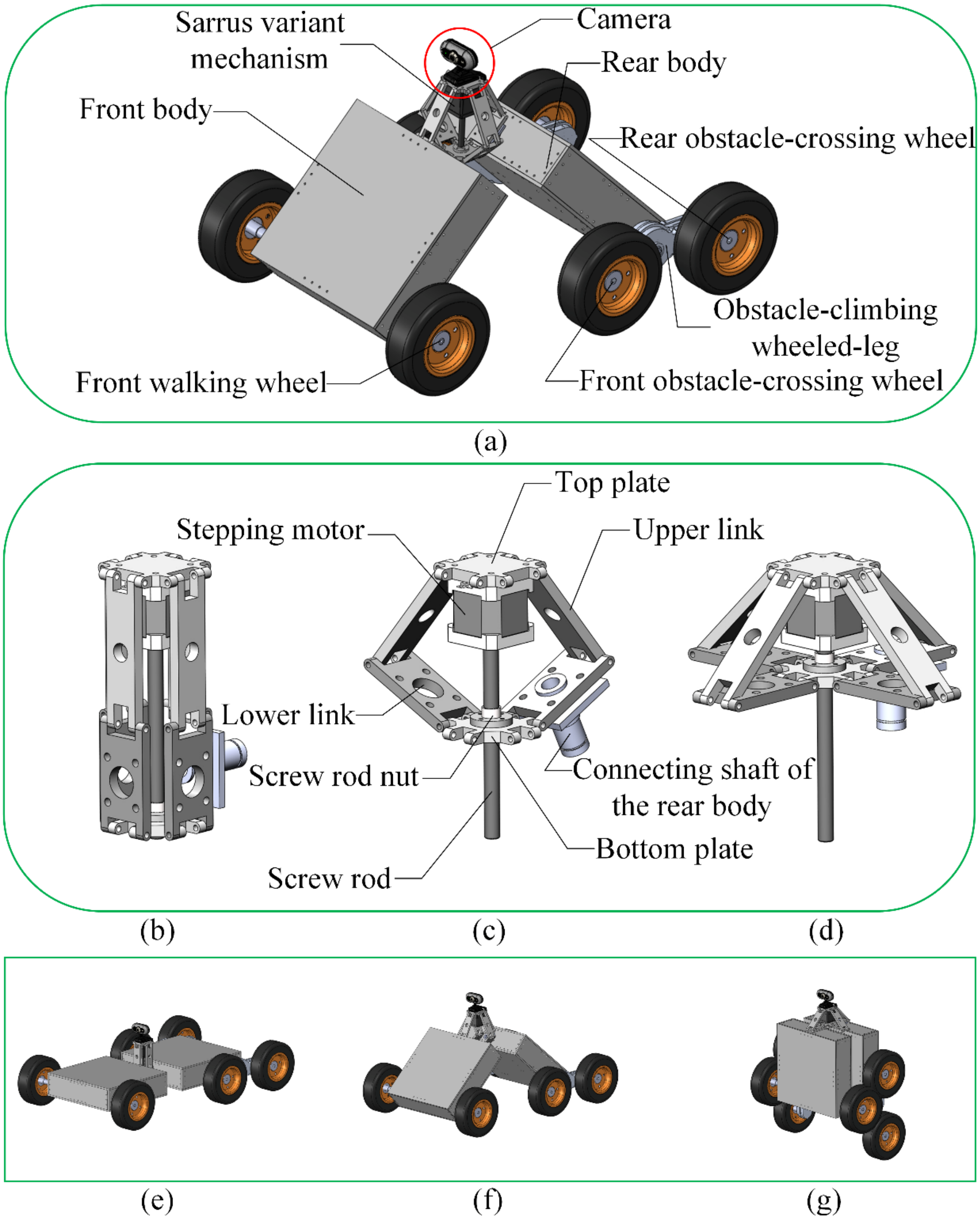
Sarrus variant mechanism
Camera
Rear body
Front body
Rear obstacle-crossing wheel
Obstacle-climbing wheeled-leg
Front walking wheel
Front obstacle-crossing wheel
(a)
Top plate
Stepping motor
Upper link
Lower link
Screw rod nut
Connecting shaft of the rear body
Bottom plate
Screw rod
(b)
(c)
(d)
(e)
(f)
(g)

Fig. 3

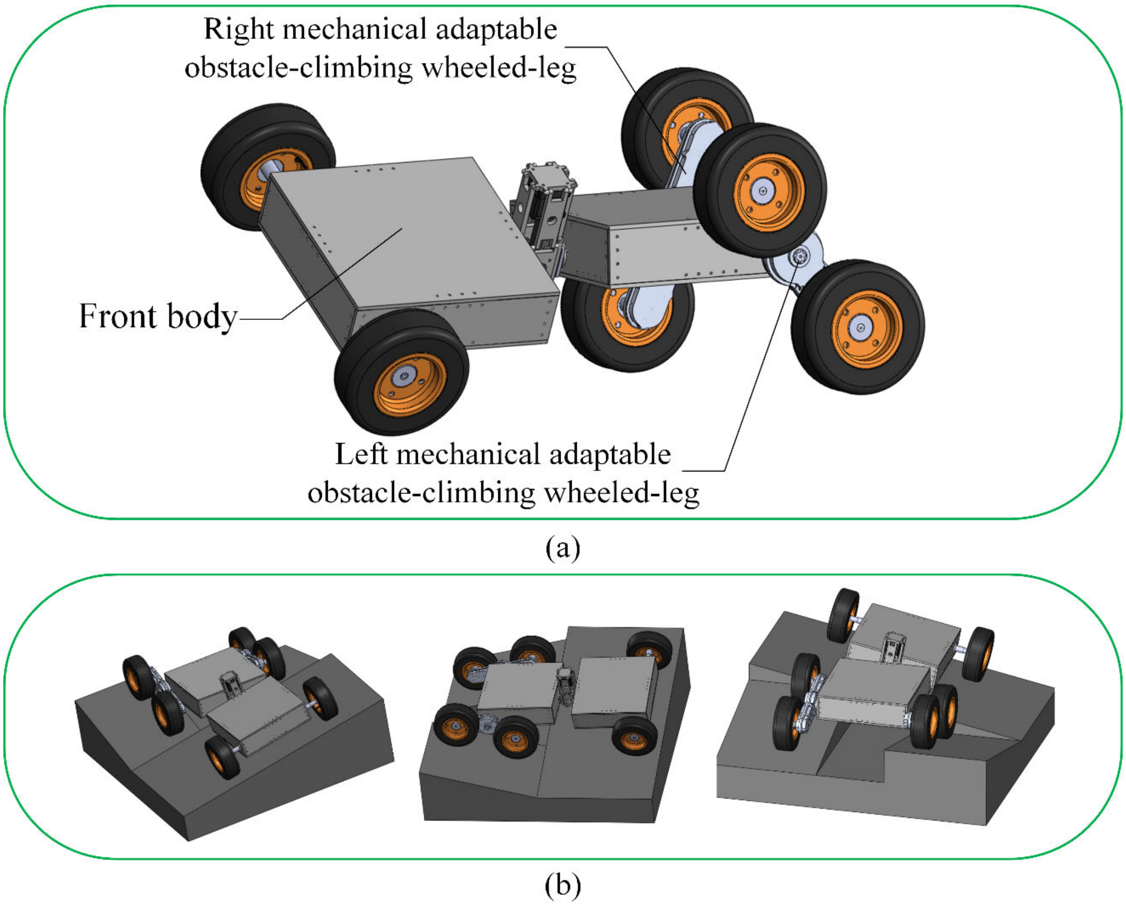
Right mechanical adaptable obstacle-climbing wheeled-leg
Front body
Left mechanical adaptable obstacle-climbing wheeled-leg
(a)
(b)

Fig. 4

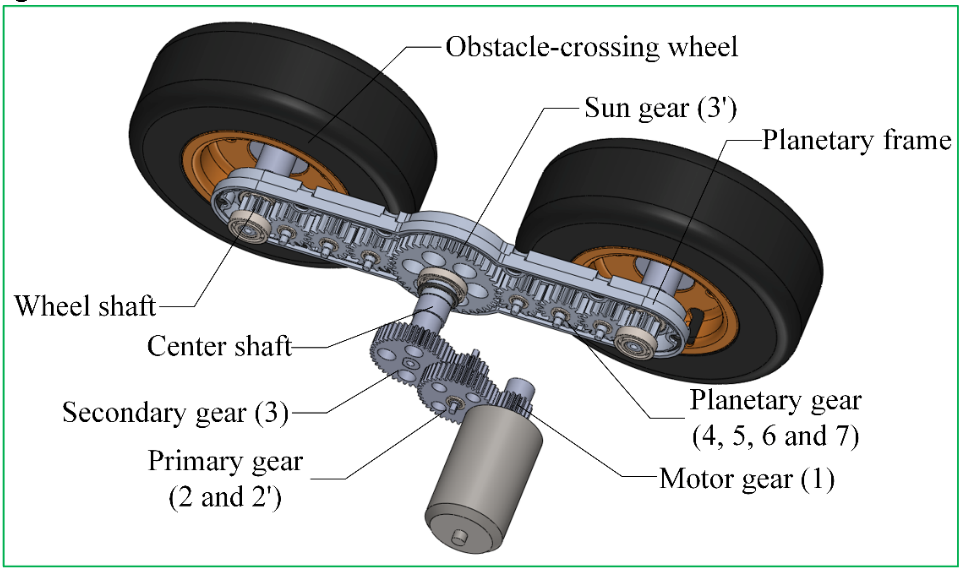

Obstacle-crossing wheel
Sun gear (3')
Planetary frame
Wheel shaft
Center shaft
Secondary gear (3)
Primary gear
(2 and 2')
Planetary gear
(4, 5, 6 and 7)
Motor gear (1)

(a)

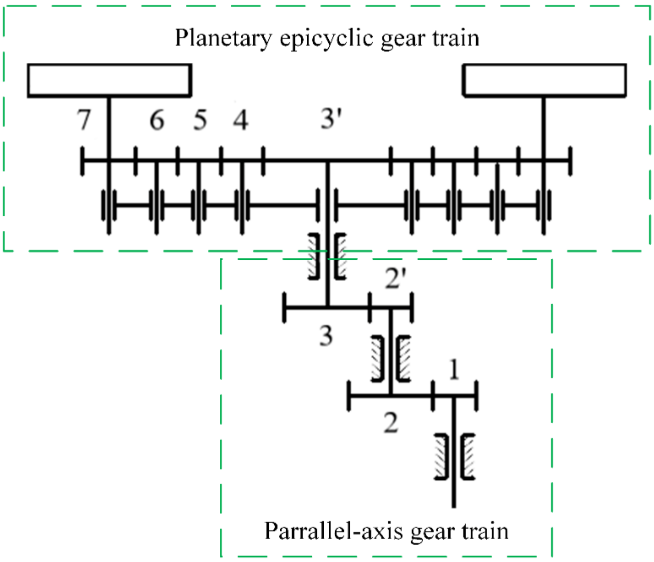

Planetary epicyclic gear train
7
6
5
4
3'
2'
3
1
2
Parrallel-axis gear train

(b)

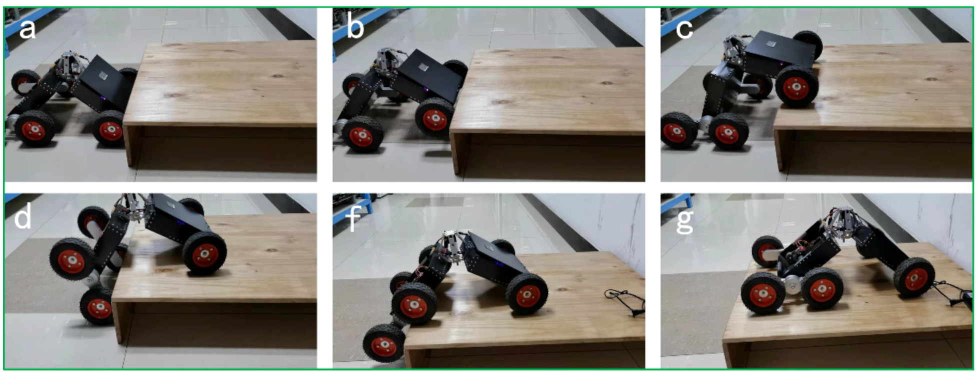

a
b
c
d
f
g

(c)

Fig .5

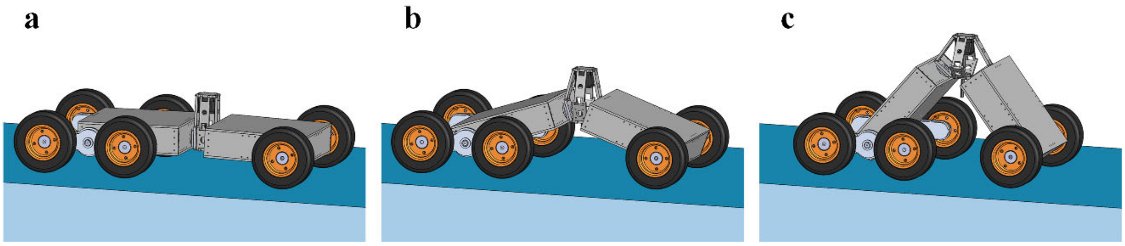

Fig .6

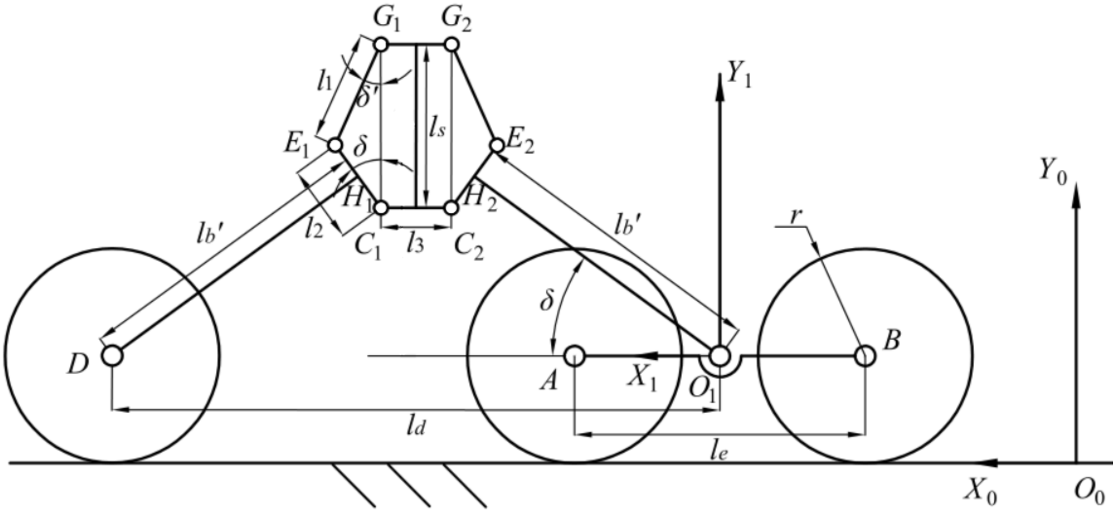

G_1
G_2
l_1
δ'
E_1
δ
l_s
E_2
Y_1
Y_0
l_b'
H_1
H_2
l_2
C_1
l_3
C_2
l_b'
r
δ
D
A
X_1
O_1
B
l_d
l_e
X_0
O_0

Fig. 7

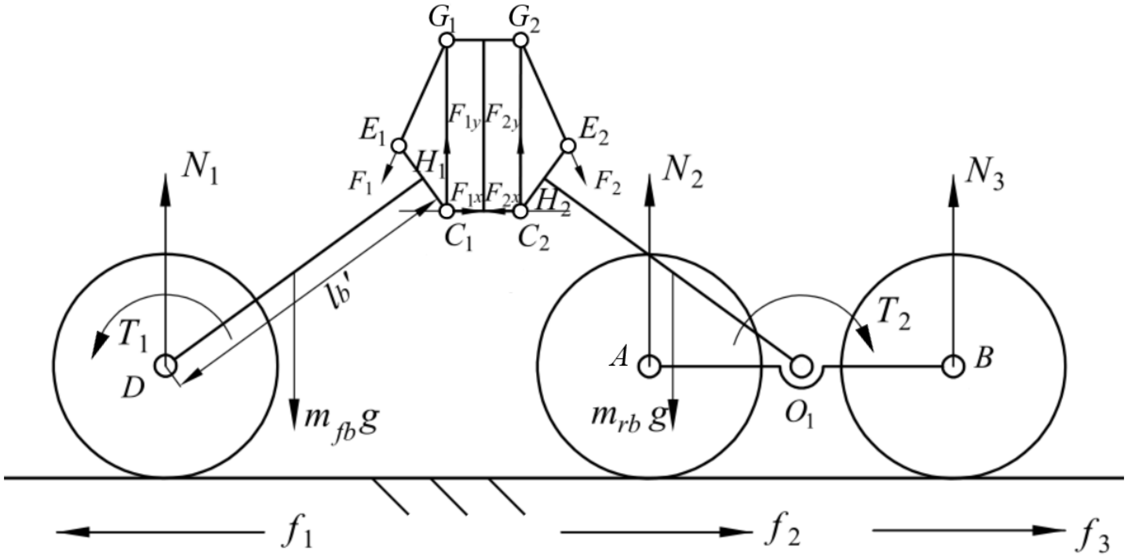

G_1
G_2
E_1
E_2
F_{1y}
F_{2y}
H_1
H_2
F_1
F_2
F_{1x}
F_{2x}
C_1
C_2
N_1
N_2
N_3
l_b'
T_1
T_2
D
A
B
O_1
$m_{fb}g$
$m_{rb}g$
f_1
f_2
f_3

Fig .8

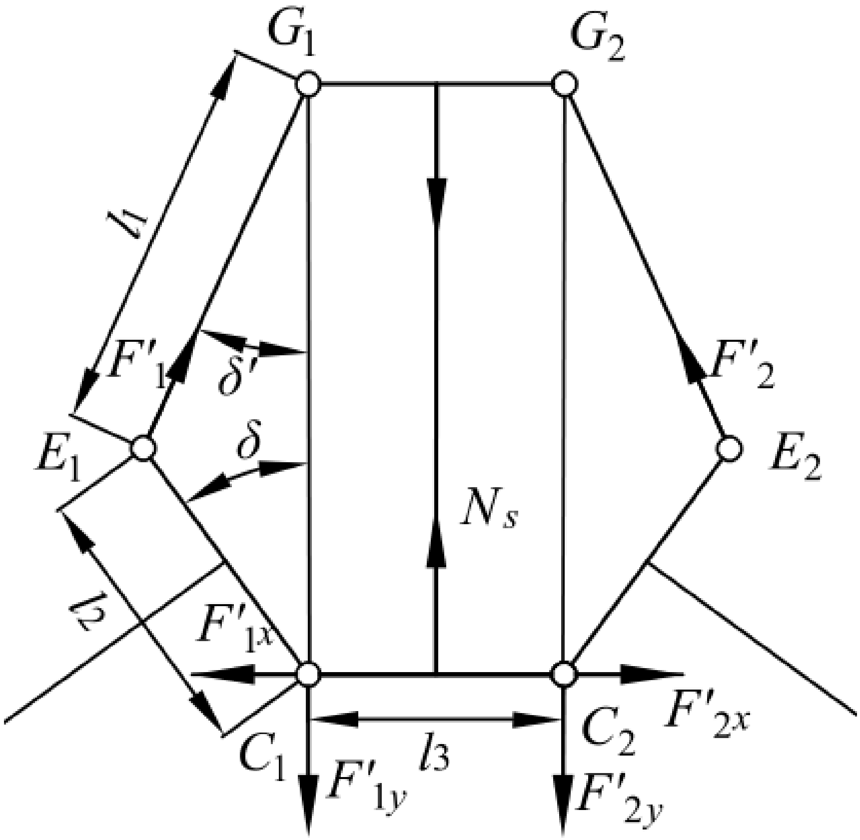

Fig .9

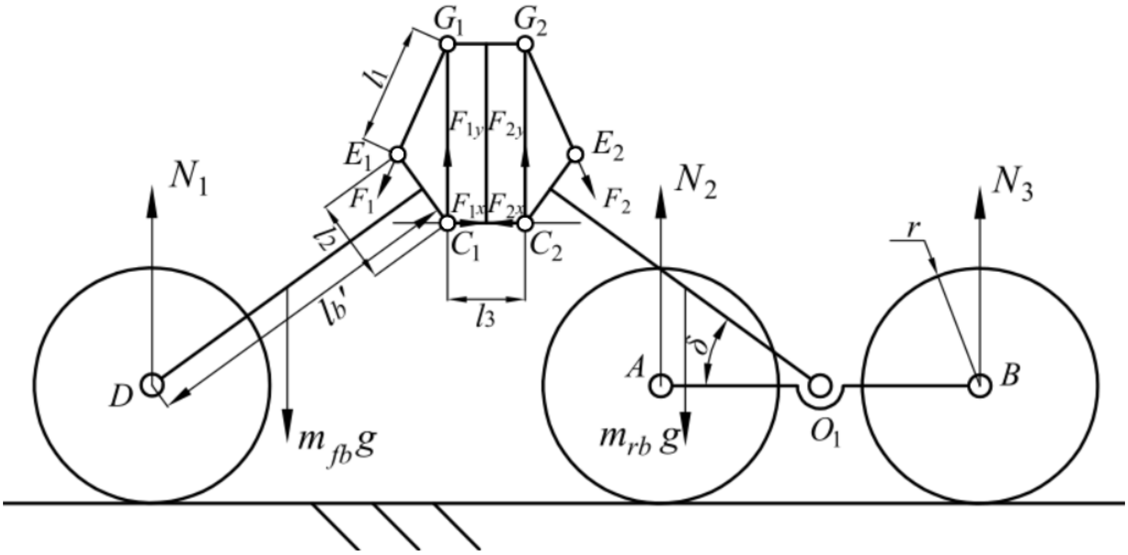

G_1
G_2
l_1
F_{1y}
F_{2y}
E_1
E_2
N_1
N_2
N_3
F_1
F_2
F_{1x}
F_{2x}
l_2
C_1
C_2
r
l_b'
l_3
δ
A
B
D
$m_{fb}g$
$m_{rb}\,g$
O_1

Fig .10

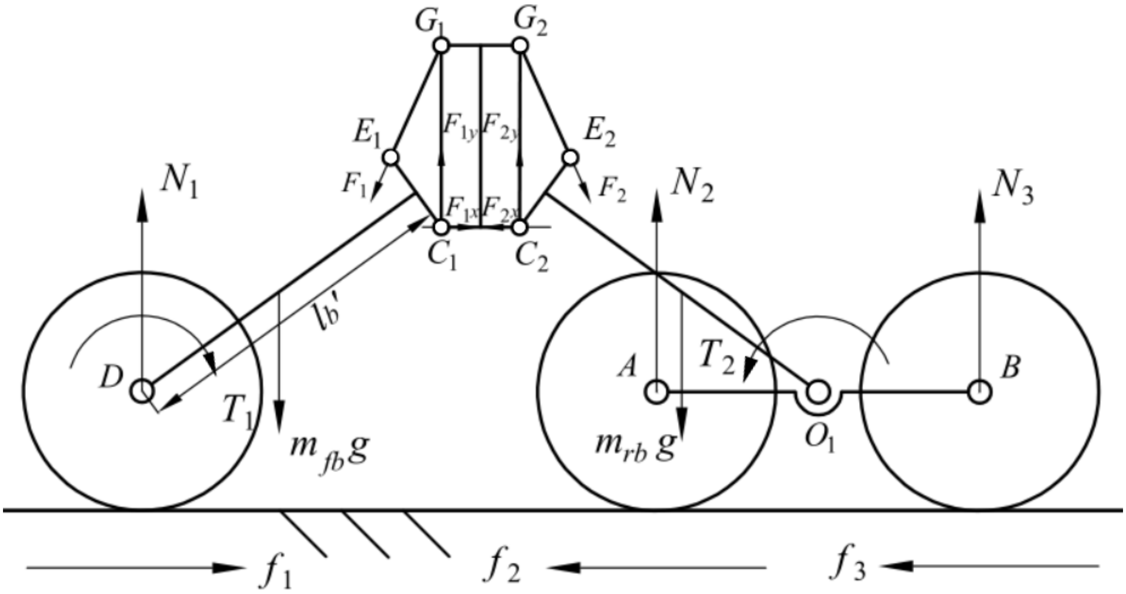
G1
G2
E1
E2
F1y
F2y
F1
F2
F1x
F2x
C1
C2
N1
N2
N3
lb'
D
A
B
O1
T1
T2
m fb g
mrb g
f1
f2
f3

Fig .11

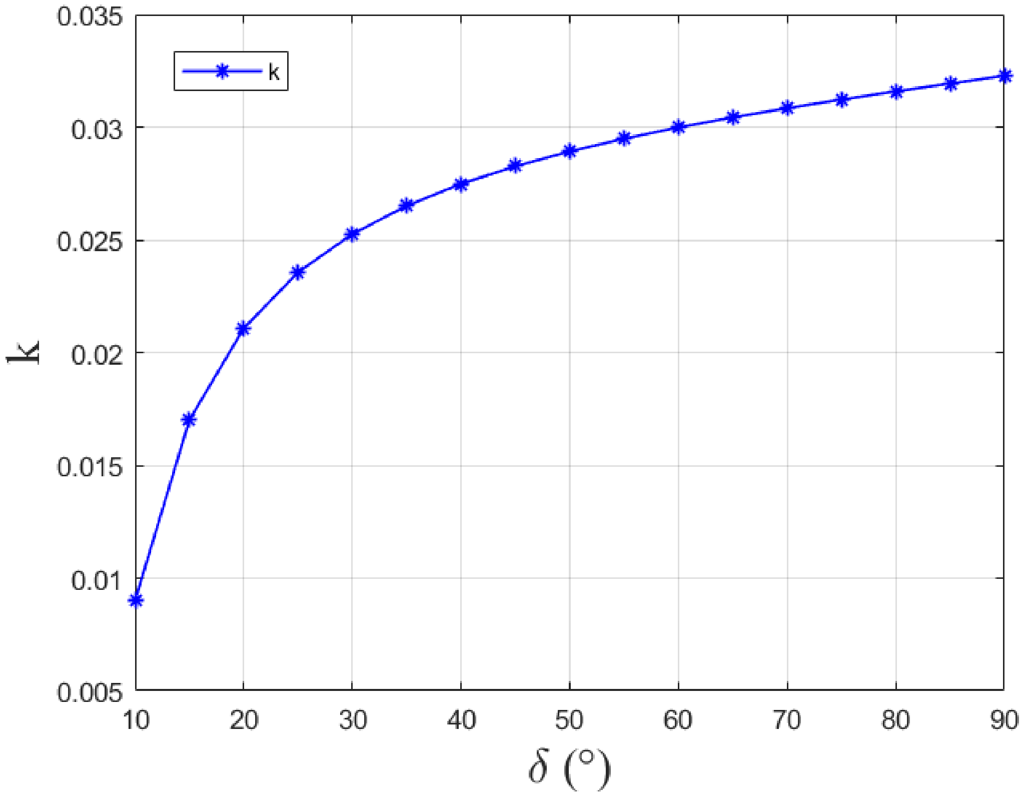

Fig. 12

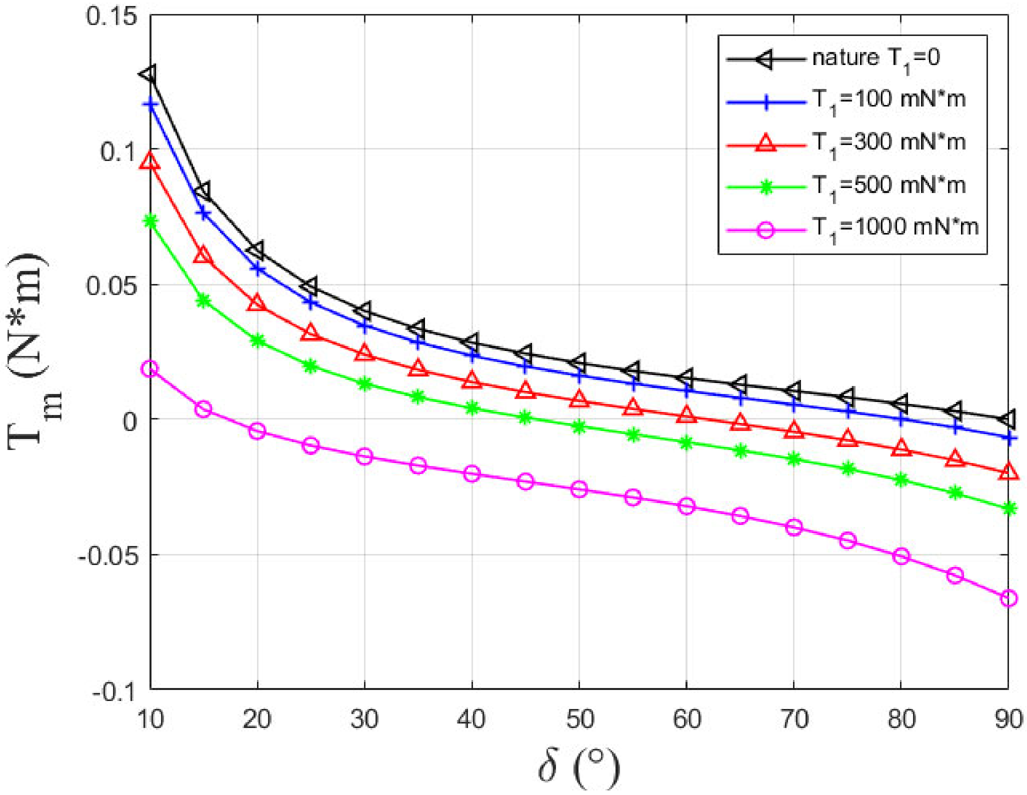

nature T1=0
T1=100 mN*m
T1=300 mN*m
T1=500 mN*m
T1=1000 mN*m
Tm (N*m)
δ (°)
0.15
0.1
0.05
0
-0.05
-0.1
10
20
30
40
50
60
70
80
90

Fig. 13

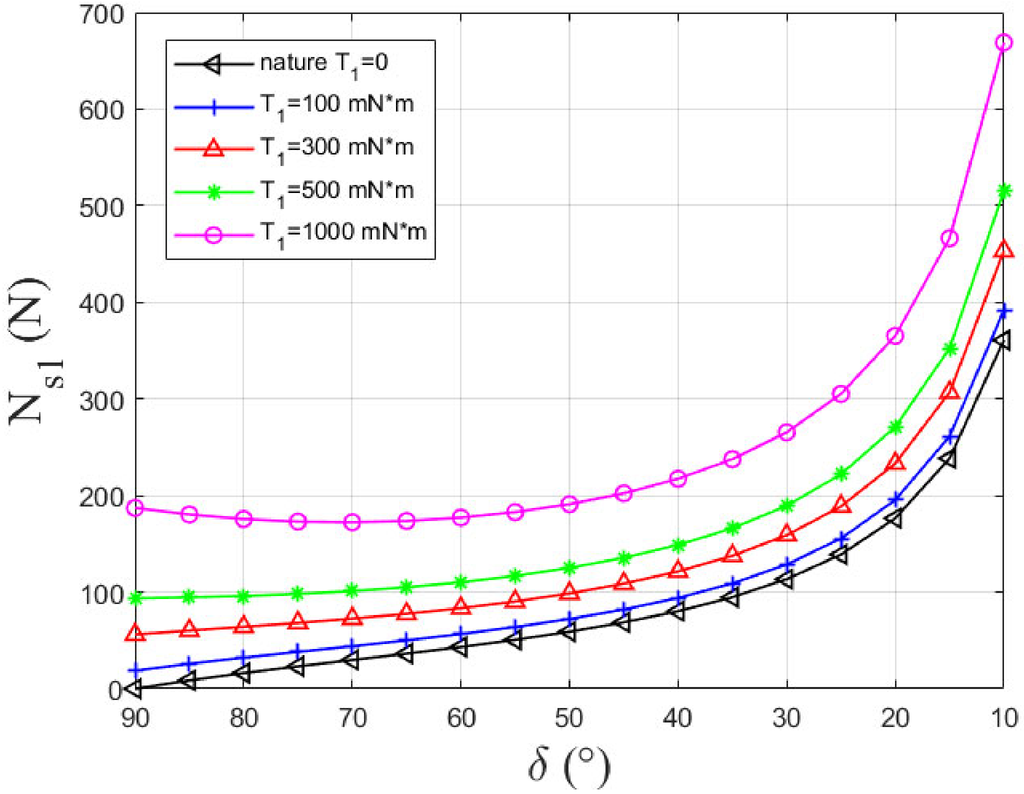
nature T1=0
T1=100 mN*m
T1=300 mN*m
T1=500 mN*m
T1=1000 mN*m
Ns1 (N)
δ (°)
0
100
200
300
400
500
600
700
90
80
70
60
50
40
30
20
10

Fig. 14

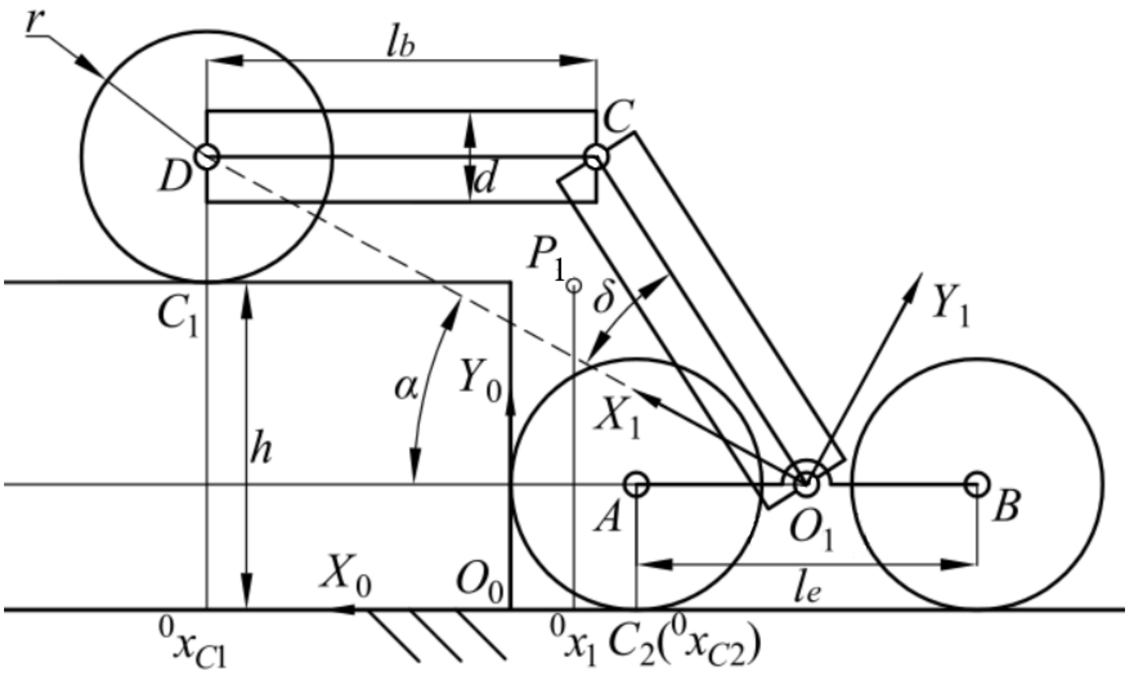

Fig. 15

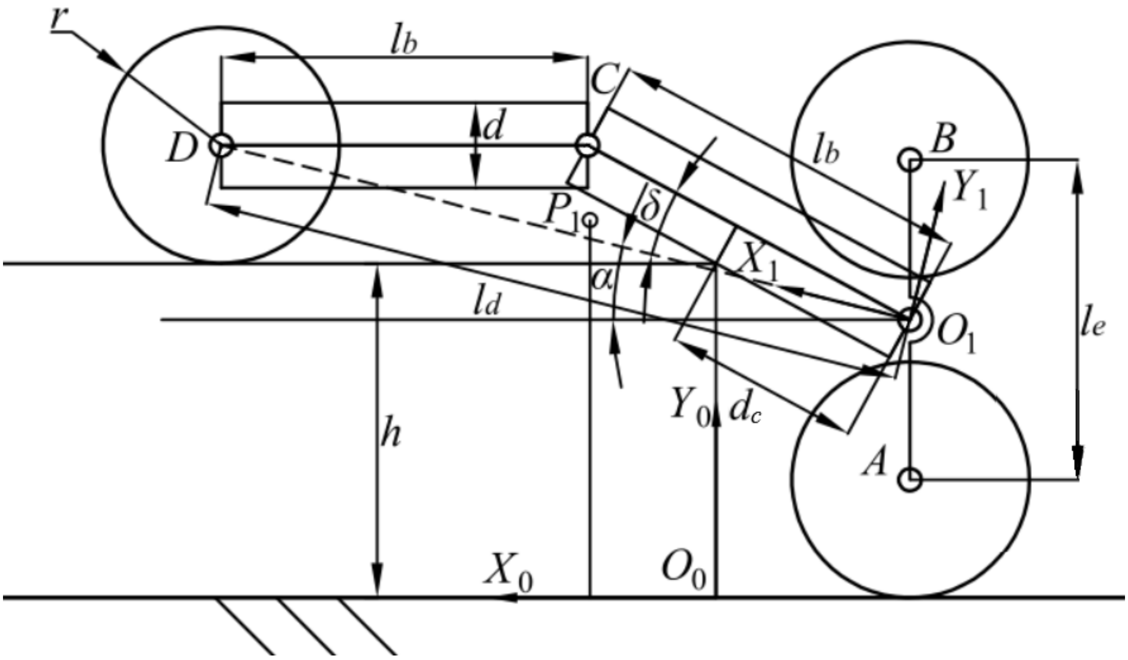

Fig. 16

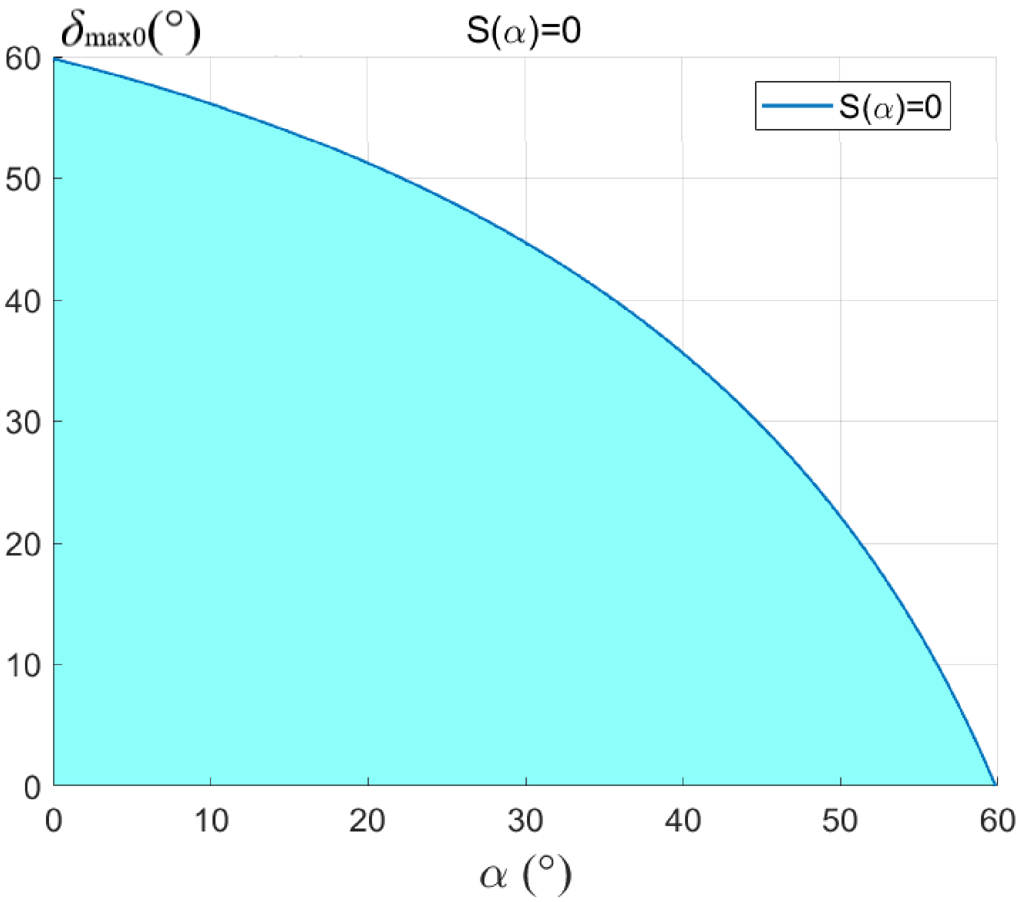

Fig. 17

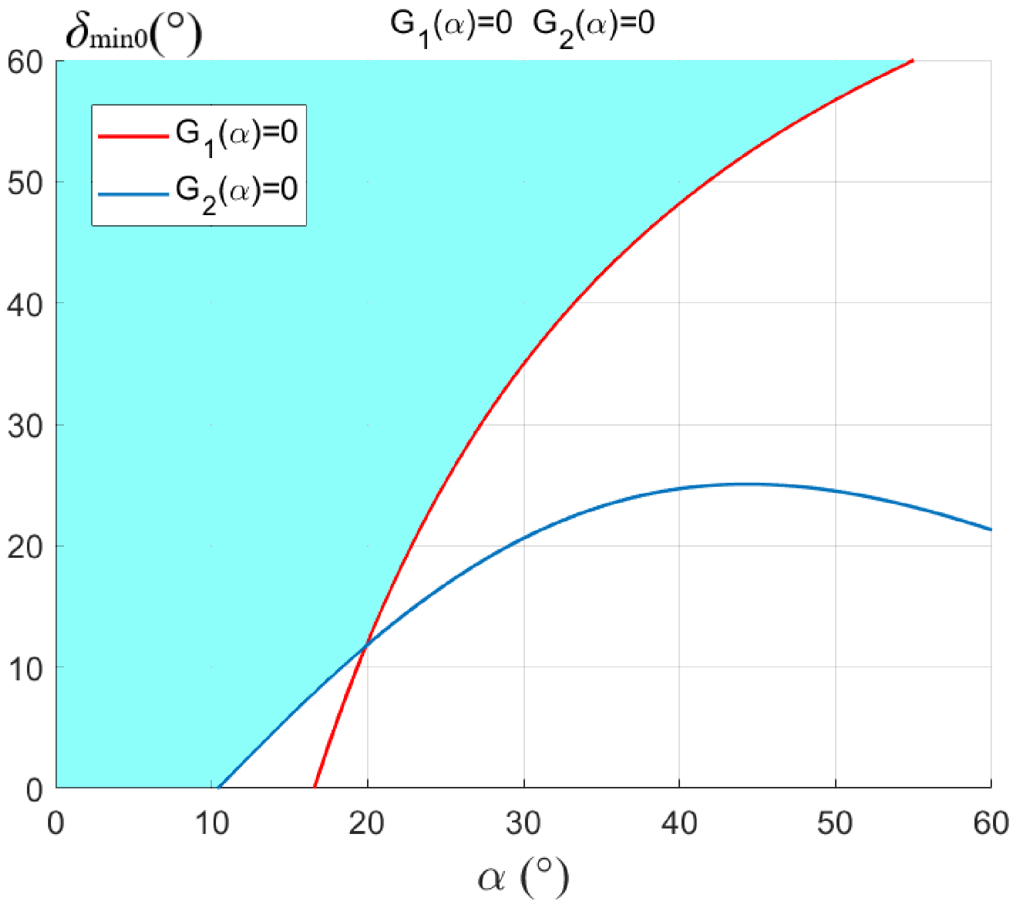
$\delta_{\min0}(°)$
G$_1$(α)=0 G$_2$(α)=0
G$_1$(α)=0
G$_2$(α)=0
60
50
40
30
20
10
0
0
10
20
30
40
50
60
α (°)

1003 Fig. 18

1004
1005

Fig. 19

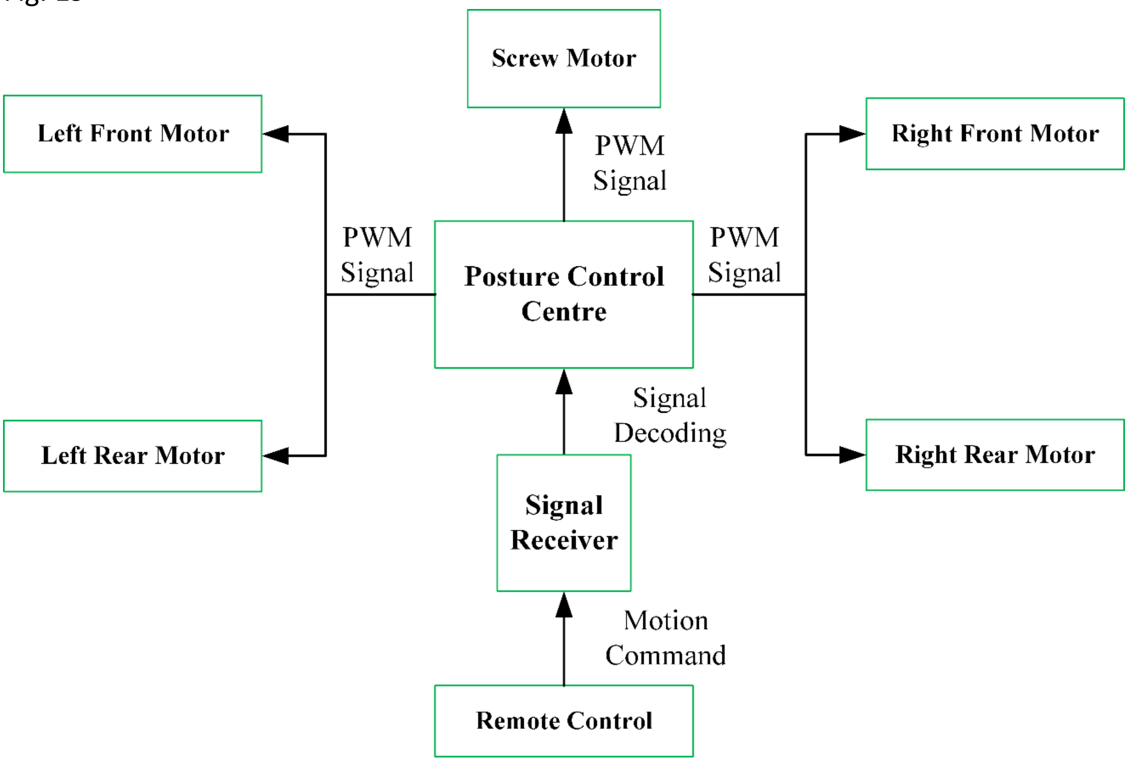
Screw Motor
Left Front Motor
Right Front Motor
PWM Signal
PWM Signal
Posture Control Centre
PWM Signal
Left Rear Motor
Signal Decoding
Right Rear Motor
Signal Receiver
Motion Command
Remote Control

Fig. 20

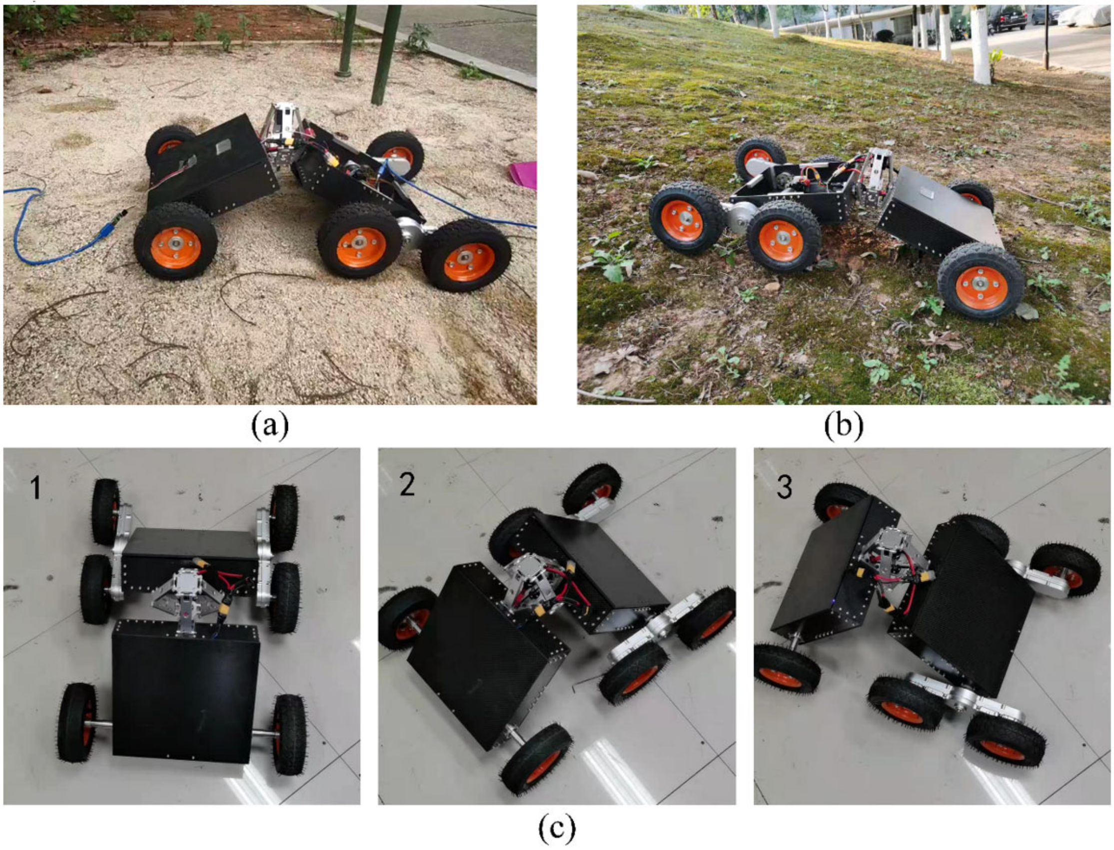

Fig. 21

Fig. 22

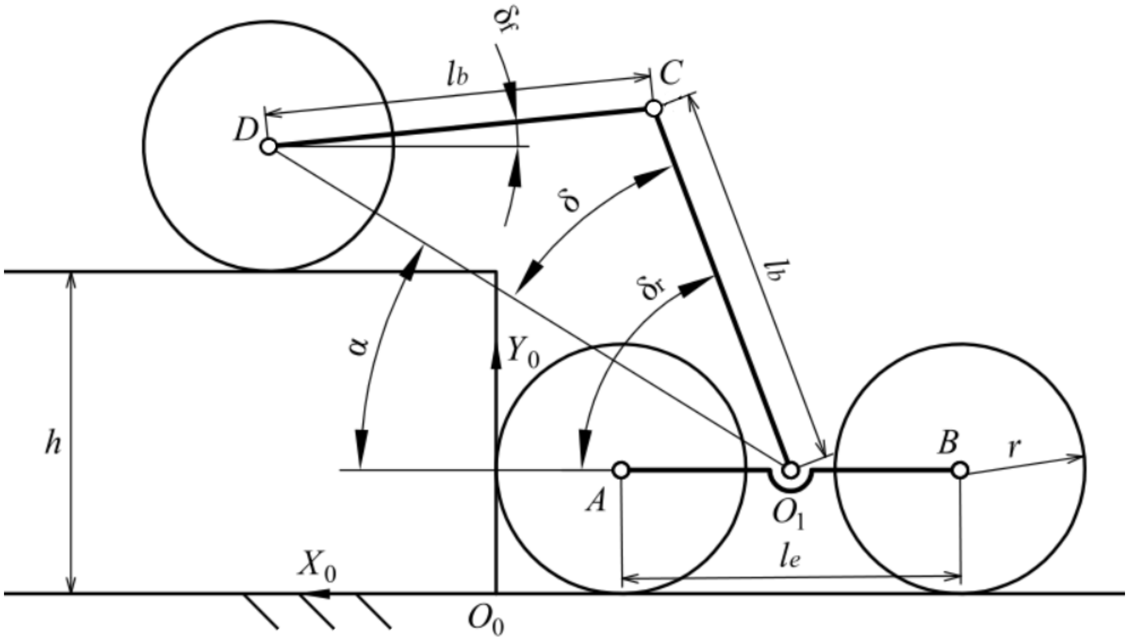

1020 Fig. 23

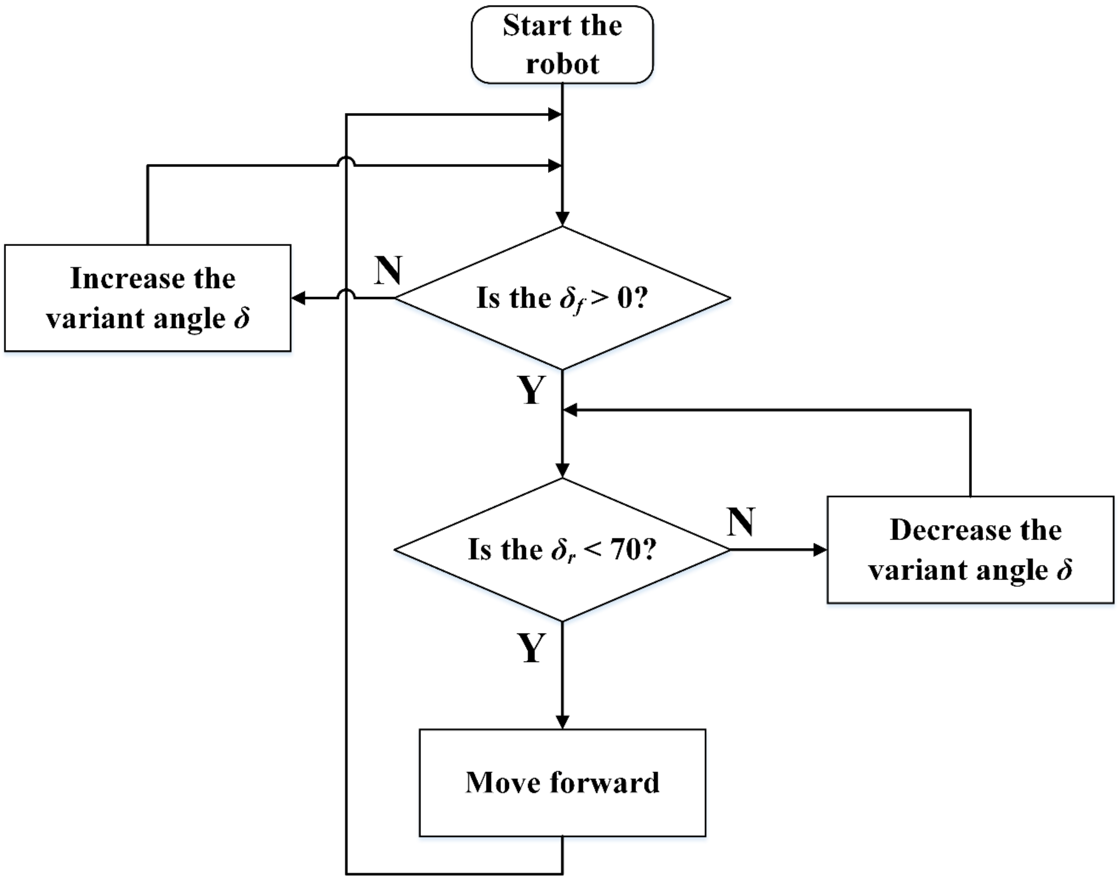

1021
1022

Fig. 24

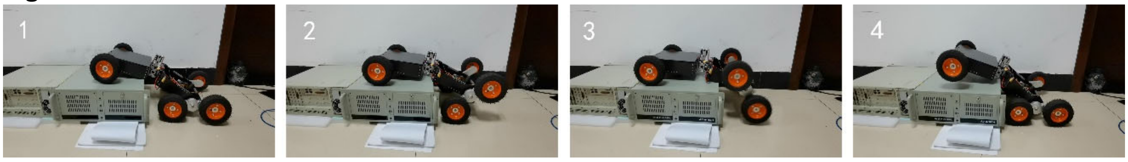

Fig. 25

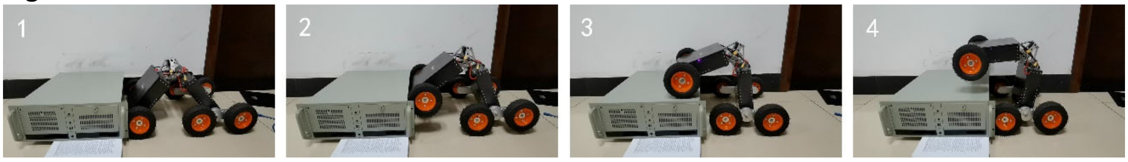

Fig. 26

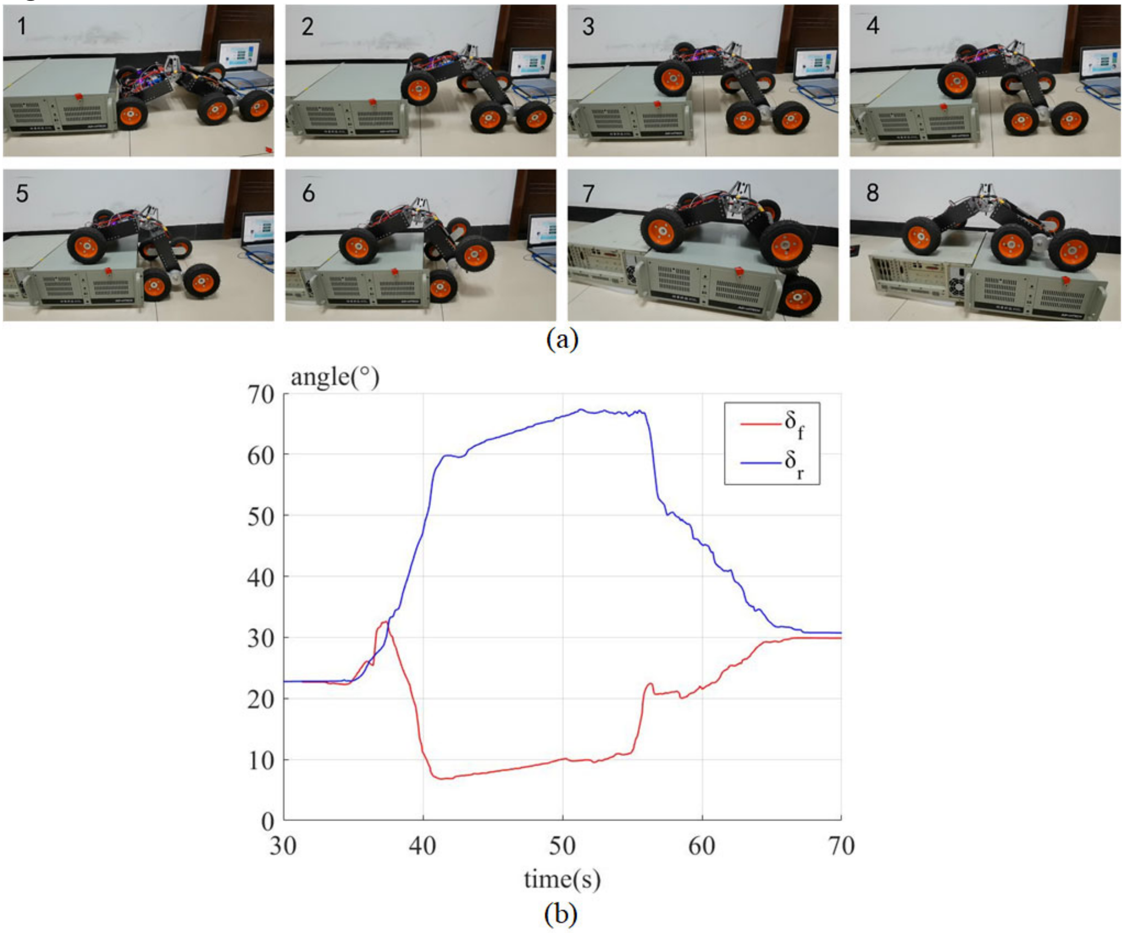

Fig. 27

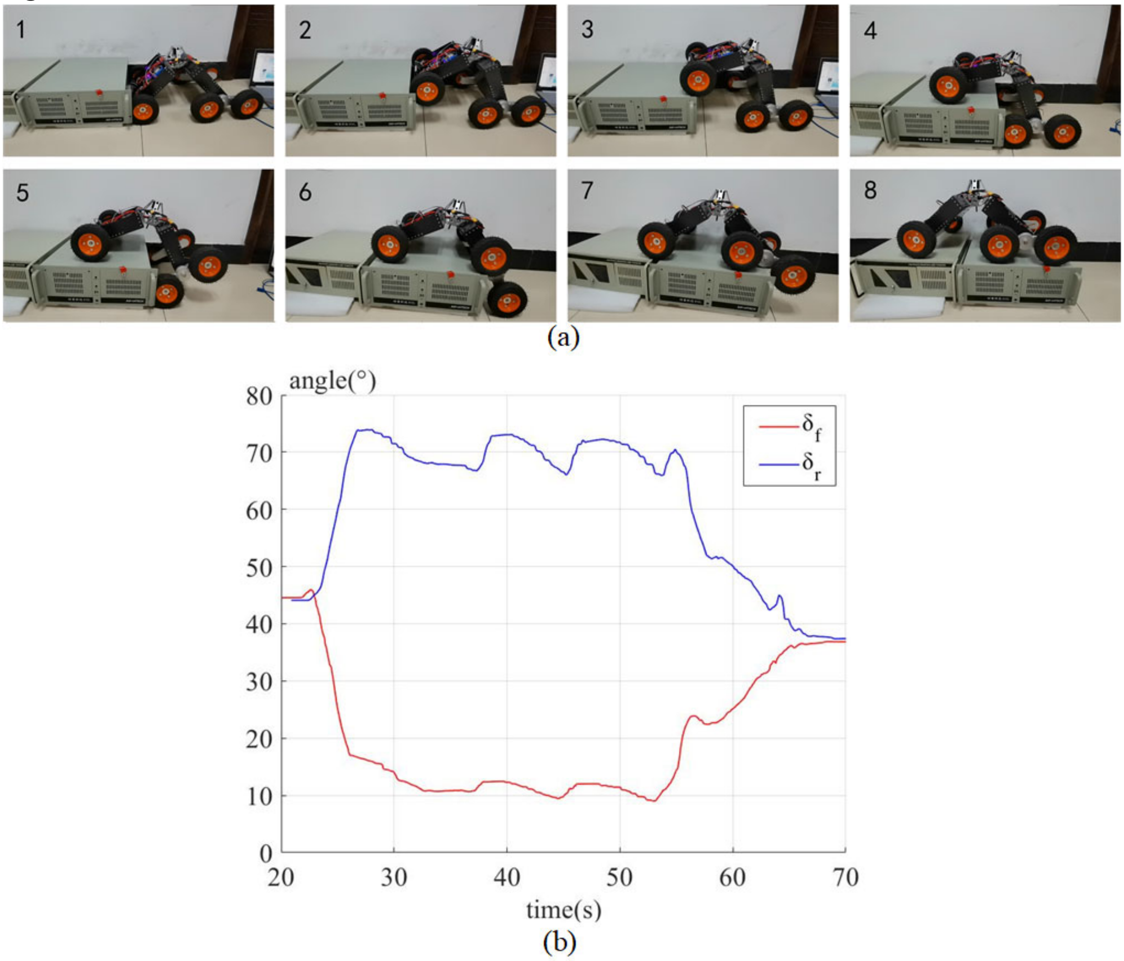
1
2
3
4
5
6
7
8
(a)
angle(°)
80
70
60
50
40
30
20
10
0
20
30
40
50
60
70
time(s)
δf
δr
(b)

Fig. 28

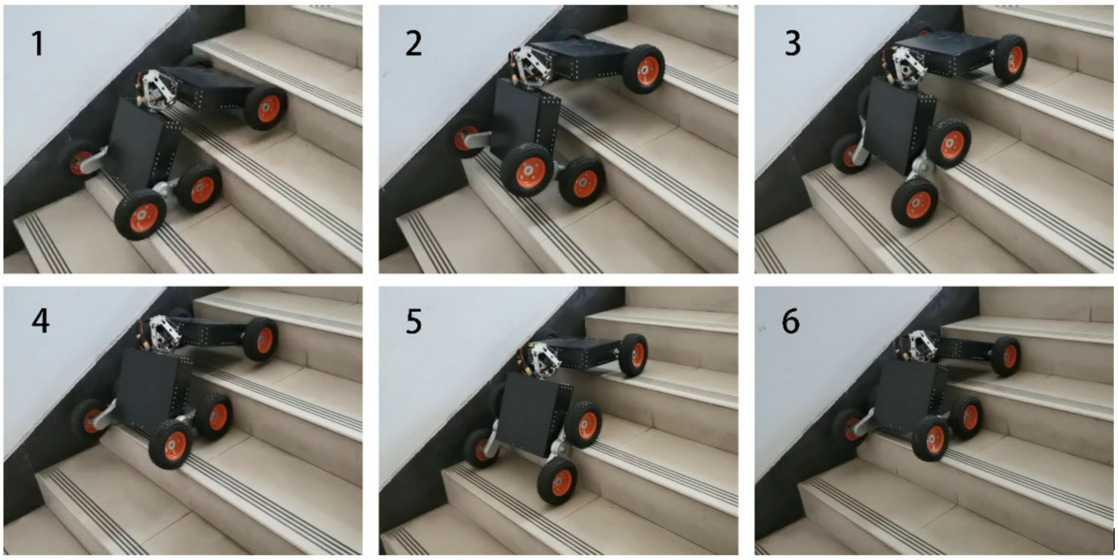

Fig. 29

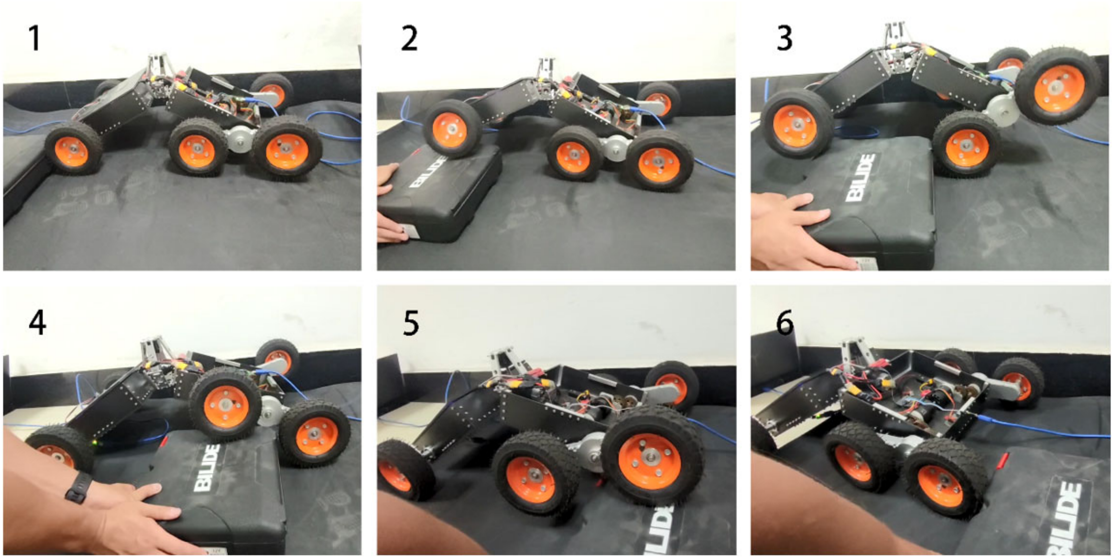

Table 1

Name	AntiBot	Epi.q-TG [32]	STEP [25, 33]	Quattroped [34, 35]	RHyMo [36-38]
Size: Length	780	450	-	600	1000
Width	454	280	-	410	700
Height	190	200	-	195(wheeled)	450
Weight	9.9 kg	4 kg	-	12.2 kg	53 kg
Radius of wheel	77.5 mm	30 mm	125 mm	107.5 mm	93 mm
Number of wheels	6	12	2	4	4
Obstacle crossing height	At least 200 mm vertical-high obstacle	About 130 mm step in friction conditions (f_s > 1.1)	At least 180 mm square stair	245 mm square step	200 mm
Transformation ratio	2.58	4.33	1.44	2.28	2.15
Obstacle crossing mechanism	Rotating wheeled-leg	Rotating wheeled-leg	Reconfigurable wheel	Reconfigurable leg-wheel	Rocker-Bogie platform with the inverse four-bar linkage mechanism
Obstacle crossing method	Autonomous adaptive obstacle crossing	Mechanical obstacle crossing	Controlled by operators	Autonomous obstacle crossing	Mechanical passive adaptive obstacle crossing

Table 2

Parameter	**Value**	**Parameter**	**Value**
m_{fb}	3.6 kg	l_b	240 mm
m_{rb}	2 kg	l_e	210 mm
m_w	0.55 kg	r	77.5 mm
m_a	1.6 kg	d	56 mm
l_1	80 mm	l_b'	220 mm
l_2	56 mm	l_3	51 mm